Global scale variability of the mineral dust longwave refractive index:

a new dataset of in situ measurements for climate modelling and remote sensing

C. Di Biagio[1], P. Formenti[1], Y. Balkanski[2], L. Caponi[1,3], M. Cazaunau[1], E. Pangui[1], E. Journet[1], S. Nowak[4], S. Caquineau[5], M. O. Andreae[6,12], K. Kandler[7], T. Saeed[8], S. Piketh[9], D. Seibert[10], E. Williams[11], and J.-F. Doussin[1]

[1] *Laboratoire Interuniversitaire des Systèmes Atmosphériques (LISA), UMR 7583, CNRS, Université Paris Est Créteil et Université Paris Diderot, Institut Pierre et Simon Laplace, Créteil, France*

[2] *Laboratoire des Sciences du Climat et de l'Environnement, CEA CNRS UVSQ, 91191, Gif sur Yvette, France*

[3] *University of Genoa, Genoa, Italy*

[4] *Plateforme RX UFR de chimie, Université Paris Diderot, Paris, France*

[5] *IRD-Sorbonne Universités (UPMC, Univ. Paris 06) – CNRS-MNHN, LOCEAN Laboratory, IRD France-Nord, F-93143 Bondy, France*

[6] *Biogeochemistry Department, Max Planck Institute for Chemistry, P.O. Box 3060, 55020, Mainz, Germany*

[7] *Institut für Angewandte Geowissenschaften, Technische Universität Darmstadt, Schnittspahnstr. 9, 64287 Darmstadt, Germany*

[8] *Science department, College of Basic Education, Public Authority for Applied Education and Training, Al-Ardeya, Kuwait*

[9] *Climatology Research Group, Unit for Environmental Science and Management, North-West University, Potchefstroom, South Africa*

[10] *Walden University, Minneapolis, Minnesota, USA*

[11] *Parsons Laboratory, Massachusetts Institute of Technology, Cambridge, Massachusetts, USA*

[12] *Geology and Geophysics Department, King Saud University, Riyadh, Saudi Arabia*

Correspondence to:

C. Di Biagio (cldibiagio@gmail.com) and P. Formenti (paola.formenti@lisa.u-pec.fr)

Abstract

Modelling the interaction of dust with longwave (LW) radiation is still a challenge ~~due to~~because of the scarcity of information on the complex refractive index of dust from different source regions. In particular, little is known ~~on~~ about the variability of the refractive index as a function of the dust mineralogical composition, ~~depending~~ which depends on the specific emission source ~~region of emission~~, and ~~the dust~~its size distribution, which is modified during transport. As a consequence, to date, climate models and remote sensing retrievals generally use a spatially-invariant and time-constant value for the dust LW refractive index.

In this paper, the variability of the mineral dust LW refractive index as a function of its mineralogical composition and size distribution is explored by in situ measurements in a large smog chamber. ~~M~~Mineral dust aerosols were generated from nineteen natural soils from Northern Africa, Sahel, Middle East, Eastern Asia, North and South America, Southern Africa, and Australia. Soil samples were selected from a total of 137 available samples ~~available~~ in order to represent the diversity of sources from arid and semi-arid areas worldwide and to account for the heterogeneity of the soil composition at the global scale. Aerosol samples generated from soils were re-suspended in the chamber, where their LW extinction spectra (2-16 µm), size distribution, and mineralogical composition were measured. The generated aerosol exhibits a realistic size distribution and mineralogy, including both the sub- and super-micron fractions, and represents in typical atmospheric proportions the main LW-active minerals, such as clays, quartz, and calcite. The complex refractive index of the aerosol is obtained by an optical inversion based upon the measured extinction spectrum and size distribution.

Results from the present study show that the imaginary LW refractive index (k) of dust varies greatly both in magnitude and spectral shape from sample to sample, ~~following the changes~~reflecting the differences in ~~the measured~~ particle composition. In the 2-16 µm spectral range, k is between ~0.001 and 0.92. The strength of the dust absorption at ~7 and 11.4 µm depends on the amount of calcite within the samples, while the absorption between 8 and 14 µm is determined by the relative abundance of quartz and clays. The imaginary part (k) is observed to vary both from region to region, as well as ~~within the same region~~ for varying sources within the same region. Conversely, for the real part (n), which is in the range 0.84-1.94, values are observed to agree for all dust samples ~~within the error bars for the most part~~across most of the spectrum within the error bars ~~for all dust samples~~. This implies that while a constant n can be probably assumed for dust from different sources, a varying k should be used both at the global and at the regional scale. ~~Results from the present study show that the LW re-~~

64 ~~fractive index of dust varies greatly both in magnitude and spectral shape from sample to sample, fol-~~

65 ~~lowing the changes in the measured particle composition. The real part (n) of the refractive index is~~

66 ~~between 0.84 and 1.94, while the imaginary part (k) is ~ 0.001 and 0.92. For instance, the strength of~~

67 ~~the absorption at ~ 7 and 11.4 µm depends on the amount of calcite within the samples, while the ab-~~

68 ~~sorption between 8 and 14 µm is determined by the relative abundance of quartz and clays.~~ A linear

69 relationship between the magnitude of the <u>imaginary</u> refractive index at 7.0, 9.2, and 11.4 µm and the

70 mass concentration of calcite and quartz absorbing at these wavelengths was found. We suggest that

71 this may lead to predictive rules to estimate the LW refractive index of dust in specific bands based on

72 an assumed or predicted mineralogical composition, or conversely, to estimate the dust composition

73 from measurements of the LW extinction at specific wavebands.

74 Based on the results of the present study, <u>we recommend that climate models and remote sensing in-</u>

75 <u>struments operating at infrared wavelengths, such as IASI (Infrared Atmospheric Sounder Interferome-</u>

76 <u>ter),</u>~~we recommend~~ us<u>ing</u>~~e~~ <u>regional-dependent</u> refractive ind<u>ex value</u>ic<u>es</u>~~ices~~ ~~specific for the different~~

77 ~~source regions,~~ rather than generic values~~, in climate models and remote sensing applications~~. Our

78 observations also suggest that the refractive index of dust in the LW does not change ~~due to~~<u>as a result</u>

79 <u>of</u> the loss of coarse particles by gravitational settling, so that ~~a~~ constant value<u>s of n and k</u> c<u>ould</u>~~ould~~ be

80 assumed close to sources and ~~during~~ <u>following</u> transport.~~ The results of the present study also clearly~~

81 ~~suggest that the~~ <u> </u>~~LW refractive index of dust varies at the regional scale. This regional variability has~~

82 ~~to be characterized further in order to better assess the influence of dust on regional climate, as well as~~

83 ~~to increase the accuracy of satellite retrievals over regions affected by dust.~~

84 ~~We make~~ <u>are making</u> ~~the whole dataset of the dust complex refractive indices obtained here available~~

85 ~~to the scientific community by publishing it in the supplementary material to this paper.~~

86 <u>The whole dataset of the dust complex refractive indices presented in this paper is made available to</u>

87 <u>the scientific community in the supplementary material.</u>

88

90

91

1. Introduction

Mis en forme : Anglais (Royaume-Uni)

93 Mineral dust is one of the most abundant aerosol species in the atmosphere and contributes significant-
94 ly to radiative perturbation, both at the regional and the global scale (Miller et al., 2014). The direct
95 radiative effect of mineral dust acts both at shortwave (SW) and longwave (LW) wavelengths (Tegen
96 and Lacis, 1996). This is due to the very large size spectrum of these particles, which extends from
97 hundreds of nanometers to tenths of micrometers, and to their mineralogy, which includes minerals
98 with absorption bands at both SW and LW wavelengths (Sokolik et al., 1998; Sokolik and Toon,
99 1999). The sub-micron dust fraction controls the interaction in the SW, where scattering is the domi-
100 nant process, while the super-micron size fraction drives the LW interaction, dominated by absorption
101 (Sokolik and Toon, 1996 and 1999). The SW and LW terms have opposite effects at the surface, Top-
102 of-Atmosphere (TOA), and within the a~~tmospher~~erosol layer~~e~~ (Hsu et al., 2000; Slingo et al., 2006).
103 ~~Indeed, t~~The dust SW effect is to cool the surface and at the TOA, and to warm the ~~atmosphere~~dust
104 layer; conversely, the dust LW effect induces a warming of the surface and TOA, and ~~a~~the~~n atmos-~~
105 ~~pheric~~ cooling of the atmospheric dust layer. The net effect of dust at the TOA is generally a warming
106 over bright surfaces (e.g.~~i.e.~~, deserts) (Yang et al., 2009) and a cooling over dark surfaces (e.g.~~i.e.~~,
107 oceans) (di Sarra et al., 2011).

108 The interaction of dust with LW radiation has ~~key~~ important implications for climate modelling and
109 remote sensing. Many studies have shown the key role of the LW effect in modulating the SW pertur-
110 bation of dust not only close to sources (Slingo et al., 2006), where the coarse size fraction is dominant
111 (Schütz et al, 1974; Ryder et al., 2013a), but also after medium- and long- range transport (di Sarra et
112 al., 2011; Meloni et al., 2015), when the larger particles (> 10 μm) were preferentially removed by wet
113 and dry deposition (Schütz et al, 1981; Maring et al., 2003; Osada et al., 2014). Thus, the dust LW
114 term has importance over the entire dust lifecycle, and has to be taken into account in order to evaluate
115 the radiative effect of dust particles on the climate system. Second, the signature of the dust LW ab-
116 sorption modifies the TOA radiance spectrum, which influences the retrieval of several climate param-
117 eters by satellite remote sensing. Misinterpretations of the data may occur if the signal of dust is not
118 accurately taken into account within satellite inversion algorithms (Sokolik, 2002; DeSouza-Machado
119 et al., 2006; Maddy et al., 2012). In addition, the dust LW signature obtained by spaceborne satellite
120 data in the 8–12 μm window region is used to estimate the concentration fields and optical depth of
121 dust (Klüser et al., 2011; Clarisse et al., 2013; Vandenbussche et al., 2013; Capelle et al., 2014; Cuesta
122 et al., 2015), with potential important applications for climate and air quality studies, health issues, and
123 visibility.

124 Currently, the magnitude and the spectral fingerprints of the dust signal in the LW are still very uncer-

125 tain. One of ~~T~~the factors ~~of~~contributing the highest uncertainty ~~come~~is ~~from~~ the poor knowledge ~~on~~

126 regarding the dust spectral complex refractive index (m= n-ik) (Claquin et al., 1998; Liao and Seinfeld,

127 1998; Sokolik et al., 1998; Highwood et al., 2003; Colarco et al., 2014). The dust complex refractive

128 index in the LW depends on the particle mineralogical composition, in particular the relative propor-

129 tion of quartz, clays (kaolinite, illite, smectite, chlorite), and calcium-rich minerals (calcite, dolomite),

130 each exhibiting specific absorption features in the LW spectrum (Sokolik et al., 1993 and 1998). Be-

131 cause of the variability of the dust composition resulting from the variability of composition of the

132 source soils (Jeong, 2008; Scheuvens et al., 2013; Formenti et al., 2014; Journet et al., 2014), atmos-

133 pheric dust produced from different regions of the world is expected to have a varying complex refrac-

134 tive index. Additional variability is expected to be introduced during transport due to the progressive

135 loss of coarse particles by gravitational settling and chemical processing (particle mixing, heterogene-

136 ous reactions, water uptake), which both change the ~~mineralogical~~ composition of the particles (Pye et

137 al., 1987; Usher et al., 2003). As a consequence, the refractive index of dust is expected to vary widely

138 at the regional and global scale.

139 Several studies have recommended taking into account the variability of the dust LW refractive index

140 in order to correctly represent its effect in climate models and satellite retrieval algorithms (Sokolik et

141 al., 1998; Claquin et al., 1999; Balkanski et al., 2007; Colarco et al., 2014; Capelle et al., 2014; among

142 others). However, to date this is precluded by the limited body of observations available. Most past

143 studies on the LW refractive index have been performed on single synthetic minerals (see Table 1 in

144 Otto et al., 2009). These data, however, are not adequate to ~~reproduce~~ represent atmospheric dust be-

145 cause of the chemical differences between the reference minerals and the minerals in the natural aero-

146 sol, and also because of the difficulty of effectively evaluating the refractive index of the dust aerosol

147 based only on information on its single constituents (e.g., McConnell et al., 2010). On the other hand,

148 very few studies have been performed on natural aerosol samples. They include the estimates obtained

149 with the KBr pellet technique by Volz (1972, 1973), Fouquart (1987), and, more recently, by Di

150 Biagio et al. (2014a), on dust samples collected at a few geographical locations (Germany, Barbados,

151 Niger, and Algeria). Besides hardly representing global dust sources, these datasets are also difficult to

152 extrapolate to atmospheric conditions as (i) they mostly refer to unknown dust mineralogical composi-

153 tion and size distribution, and also (ii) are obtained from analyses of field samples that might have ex-

154 perienced unknown physico-chemical transformations. In addition, they have a rather coarse spectral
155 resolution, which is sometimes insufficient to resolve the main dust spectral features.

156 As a consequence, climate models and satellite retrievals presently use a spatially-invariant and time-
157 constant value for the dust LW refractive index (e.g., Miller et al., 2014; Capelle et al., 2014), implicit-
158 ly assuming a uniform as well as transport- and processing-invariant dust composition.

159 Recently, novel data of the LW refractive index for dust from the Sahara, the Sahel, and the Gobi de-
160 serts have been obtained from in situ measurements in a large smog chamber (Di Biagio et al., 2014b;
161 hereinafter DB14). These measurements were performed in the realistic and dynamic environment of
162 the 4.2 m^3 CESAM chamber (French acronym for Experimental Multiphasic Atmospheric Simulation
163 Chamber) (Wang et al., 2011), using a validated generation mechanism to produce mineral dust from
164 parent soils (Alfaro et al., 2004). The mineralogical composition and size distribution of the particles
165 were measured along with the optical data, thus providing a link between particle physico-chemical
166 and optical properties.

167 In this study, we review, optimize, and extend the approach of DB14 to investigate the LW optical
168 properties of mineral dust aerosols from nineteen soils from major source regions worldwide, in order
169 to: (i) characterize the dependence of the dust LW refractive index on the particle origin and different
170 mineralogical compositions; and (ii) investigate the variability of the refractive index as a function of
171 the change in size distribution that may occur during medium- and long-range transport.

172 The paper is organized as follows: in Sect. 2 we describe the experimental set-up, instrumentation and
173 data analysis, while in Sect. 3 the algorithm to retrieve the LW complex refractive index from observa-
174 tions is discussed. Criteria for soil selection and their representativeness of the global dust are dis-
175 cussed in Sect. 4. Results are presented in Sect. 5. At first, the atmospheric representativeness in terms
176 of mineralogy and size distribution of the generated aerosols used in the experiments is evaluated
177 (Sect. 5.1 and 5.2), then the extinction and complex refractive index spectra obtained for the different
178 source regions and at different aging times in the chamber are presented in Sect. 5.3. The discussion of
179 the results, ~~their~~ a comparison with the literature, and the main conclusions are given in Sect. 6 and 7.

180

181 **2. Experimental set-up and instrumentation**

The schematic configuration of the CESAM chamber set-up for the dust experiments is shown in Fig. 1. Prior to each experiment, the chamber was evacuated and kept at a pressure of $3 \cdot 10^{-4}$ hPa. Then, the reactor was filled with a mixture of 80% N_2 (produced by evaporation from a pressurized liquid nitrogen tank, Messer, purity >99.995%) and 20% O_2 (Linde, 5.0). The chamber was equipped with a four-blade stainless steel fan to achieve homogeneous conditions within the chamber volume (with a typical mixing time of approximately 1 minute). Mineral dust aerosols generated from parent soils were dispersed into the chamber and left in suspension for a time period of 60-120 min, whilst monitoring the evolution of their physico-chemical and optical properties. The LW spectrum of the dust aerosols was measured by means of an in situ FTIR. Concurrently, the particle size distribution and the SW scattering, absorption and extinction coefficients were measured by several instruments sampling aerosols from the chamber. They include a scanning mobility particle sizer (SMPS, and WELAS and SkyGrimm optical particle counters for the size distribution, and a nephelometer (TSI Inc. model 3563), an aethalometer (Magee Sci. model AE31), and two Cavity Attenuated Phase Shift Extinction (CAPS PMeX by Aerodyne) for aerosol SW optical properties. Dust samples were also collected on polycarbonate filters over the largest part of each experiment (47-mm Nuclepore, Whatman, nominal pore size 0.4 μm) for an analysis of the particle mineralogical composition averaged over the length of the experiment.

The inlets for sampling aerosols from the chamber (for size and SW optics measurements and filter sampling) consisted of two parts: 1) a stainless steel tube (~20-40 cm length, 9.5 mm diameter) located inside CESAM, which extracted air from the interior of the chamber, and 2) an external connection from the chamber to the instruments. All external connections were made using 0.64 cm conductive silicone tubing (TSI Inc.) to minimize particle loss by electrostatic deposition. The sampling lines were designed to be as straight and as short as possible, and their total length varied between 40 and 120 cm. The possible losses as a function of particle diameter were carefully estimated for each inlet and the related data properly corrected (Sect. 2.3.2). To compensate for the air being extracted from the chamber by the various instruments, a particle-free N_2/O_2 mixture was continuously injected into the chamber.

All experiments were conducted at ambient temperature and relative humidity <2%. The chamber was manually cleaned between the different experiments to avoid any carryover contaminations as far as possible. Background concentrations of aerosols in the chamber varied between 0.5 and 2.0 μg m^{-3}.

212 In the following paragraphs we describe the system for dust generation, measurements of the dust LW
213 spectrum, size distribution, and mineralogy, and data analysis. A summary of the different measured
214 and retrieved quantities in this study and their estimated uncertainties is reported in Table 1. Longwave
215 optical and size distribution data, acquired ~~with~~ at different temporal resolutions, are averaged over 10-
216 min intervals. Uncertainties on the average values are obtained as the standard deviation over the 10-
217 min intervals.

218 A full description of the SW optical measurements and results is out of the scope of the present study
219 and will be provided in a forthcoming paper (Di Biagio et al., in preparation).

220

221 2.1 Dust aerosol generation

222 In order to mimic the natural emission process, dust aerosols were generated by mechanical shaking of
223 natural soil samples, as described in DB14. The soils used in this study consist of the surface layer,
224 which is subject to wind erosion in nature (Pye et al., 1987). Prior to each experiment, the soil samples
225 were sieved to <1000 μm and dried at 100 °C for about 1 h to remove any residual humidity. This pro-
226 cessing did not affect the mineral crystalline structure of the soil (Sertsu and Sánchez, 1978).

227 About 15 g of soil sample was placed in a Büchner flask and shaken for about 30 min at 100 Hz by
228 means of a sieve shaker (Retsch AS200). The dust suspension in the flask was then injected into the
229 chamber by flushing it with N_2 at 10 L min^{-1} for about 10-15 min, whilst continuously shaking the soil.
230 Larger quantities of soil sample (60 g) mixed with pure quartz (60 g) had been used in DB14 to max-
231 imize the concentrations of the generated dust. The presence of the pure quartz grains increases the
232 efficiency of the shaking, allowing a rapid generation of high dust concentrations. In that case it had
233 been necessary, however, to pass the aerosol flow through a stainless steel settling cylinder to ~~avoid~~
234 prevent large quartz grains from entering the chamber (DB14). For the present experiments, the gener-
235 ation system was optimized, i.e., the mechanical system used to fix the flask to the shaker was im-
236 proved so that the soil shaking was more powerful, and sufficient quantities of dust aerosols could be
237 generated by using a smaller amount of soil and without adding quartz to the soil sample. In this way,
238 the settling cylinder could be eliminated. No differences were observed in the size distribution or min-
239 eralogy of the generated dust between the two approaches.

240

2.2 LW optical measurements: FTIR extinction spectrum

The extinction spectrum of dust aerosols in the longwave was measured by means of an in situ Fourier Transform Infrared spectrometer (FTIR) (Bruker® Tensor 37[TM]) analytical system. The spectrometer is equipped with a liquid nitrogen-cooled Mercury Cadmium Telluride (MCT) detector and a Globar source. The FTIR measures between wavelengths of 2.0 μm (5000 cm^{-1}) and 16 μm (625 cm^{-1}) at 2 cm^{-1} resolution (which corresponds to a resolution varying from about 0.0008 μm at 2.0 μm wavelength to 0.05 μm at 16 μm) by co-adding 158 scans over 2 minutes. The FTIR is interfaced with a multi-pass cell to achieve a total optical path length (x) within the chamber of 192 ± 4 m. The FTIR reference spectrum was acquired immediately before the dust injection. In some cases small amounts of water vapor and CO_2 entered CESAM during particle injection and partly contaminated the dust spectra below 7 μm. This did not influence the state of particles as the chamber remained very dry (relative humidity < 2%). Water vapor and CO_2 absorption lines were carefully subtracted using reference spectra. The measured spectra were then interpolated at 0.02 μm wavelength resolution (which corresponds to a resolution varying from about 0.8 cm^{-1} at 625 cm^{-1} wavenumber to 50 cm^{-1} at 5000 cm^{-1}). Starting from the FTIR measured transmission (T), the dust spectral extinction coefficient β_{ext} in the 2-16 μm range was calculated as:

$$\beta_{ext}(\lambda) = \frac{-\ln(T(\lambda))}{x} . \quad (1)$$

The uncertainty on β_{ext} was calculated with the error propagation formula by considering the uncertainties arising from T noise (~1%) and from the standard deviation of the 10-min averages and of the path length x. We estimated it to be ~10%.

In the 2-16 μm range, the dust extinction measured by the FTIR is due to the sum of scattering and absorption. Scattering dominates below 6 μm, while absorption is dominant above 6 μm. The FTIR multipass cell in the CESAM chamber has been built following the White (1942) design (see Fig. 1). In this configuration, a significant fraction of the light scattered by the dust enters the FTIR detector and is not measured as extinction. This is because mineral dust is dominated by the super-micron fraction, which scatters predominantly in the forward direction. As a consequence, the FTIR signal in the presence of mineral dust will represent only a fraction of dust scattering below 6 μm and almost exclusively absorption above 6 μm. Figure S1 (supplementary material), shows an example of the angular distribution of scattered light (phase function) and the scattering-to-absorption ratio calculated as a

270 function of the wavelength in the LW for one of the samples used in this study. ~~R~~The results of the
271 calculations confirm that above 6 µm the scattering signal measured by the FTIR accounts for less than
272 20% of the total LW extinction at the peak of the injection and less than 10% after 120 minutes in the
273 chamber. Consequently, we approximate Eq. (1) as:

274
$$\beta_{abs}(\lambda) \approx \frac{-\ln(T(\lambda))}{x} \quad (\lambda > 6 \text{ µm}). \qquad (2)$$

275

276 **2.3 Size distribution measurements**

277 The particle number size distribution in the chamber was measured with several instruments, based on
278 different principles and operating in different size ranges:~~-~~

279 - a scanning mobility particle sizer (SMPS) (TSI, DMA Model 3080, CPC Model 3772; operated at
280   2.0/0.2 L min^{-1} sheath/aerosol flow rates; ~~2 min~~135-sec resolution), measuring the dust electrical
281   mobility diameters (D_m, i.e., the diameter of a sphere with the same migration velocity in a con-
282   stant electric field as the particle of interest) in the range 0.019–0.882 µm. Given that dust parti-
283   cles have a density larger than unity (assuming an effective density of 2.5 g cm^{-3}), the cut point
284   of the impactor at the input of the SMPS shifts towards lower diameters. This reduces the range
285   of measured mobility diameters to ~0.019-0.50 µm. The SMPS was calibrated prior the cam-
286   paign with PSL particles (Thermo Sci.) of 0.05, 0.1, and 0.5 µm nominal diameters;

287 - a WELAS optical particle counter (PALAS, model 2000; white light source between 0.35-0.70 µm;
288   flow rate 2 L min^{-1}; 60~~1 min~~sec resolution), measuring the dust sphere-equivalent optical diame-
289   ters (D_{opt}, i.e., the diameter of a sphere yielding on the same detector geometry the same optical
290   response as the particle of interest) in the range 0.58-40.7 µm. The WELAS was calibrated prior
291   the campaign with Caldust 1100 (Palas) reference particles;

292 - a SkyGrimm optical particle counter (Grimm Inc., model 1.129; 0.655 µm operating wavelength;
293   flow rate 1.2 L min^{-1}; 6-sec resolution), measuring the dust sphere-equivalent optical diameters
294   (D_{opt}) in the range 0.25-32 µm. The SkyGrimm was calibrated after the campaign against a
295   "master" Grimm (model 1.109) just recalibrated at the factory.

296 The SMPS and the WELAS were installed at the bottom of the chamber, while the SkyGrimm was
297 installed at the top of the chamber on the same horizontal plane as the FTIR spectrometer and at about

10

298 60 cm across the chamber from the WELAS and the SMPS. As already discussed in DB14, measure-
299 ments at the top and bottom of the chamber ~~are~~ were in very good agreement during the whole dura-
300 tion of each experiment, which indicates a good homogeneity of the dust aerosols in the chamber.

301

302 **2.3.1 Corrections of SMPS, WELAS, and SkyGrimm data**

303 Different corrections have to be applied to the instruments measuring the particle size distribution. For
304 the SMPS, corrections for particle loss by diffusion in the instrument tubing and the contribution of
305 multiple-charged particles were performed using the SMPS software. The electrical mobility diameter
306 measured by the SMPS was converted to a geometrical diameter (D_g) by taking into account the parti-
307 cle dynamic shape factor (χ), as $D_g = D_m / \chi$. The shape factor χ, determined by comparison with the
308 SkyGrimm in the overlapping particle range (~0.25-0.50 µm), was found to be 1.75±0.10. This value
309 is higher than those reported in the literature for mineral dust (1.1-1.6; e.g., Davies, 1979; Kaaden et
310 al., 2008). The uncertainty in D_g was estimated with the error propagation formula and was ~6%.

311 For the WELAS, optical diameters were converted to sphere-equivalent geometrical diameters (D_g) by
312 taking into account the visible complex refractive index. The D_{opt} to D_g diameter conversion was per-
313 formed based on the range of values reported in the literature for dust in the visible range, i.e., 1.47–
314 1.53 for the real part and 0.001–0.005 for the imaginary part (Osborne et al., 2008; Otto et al., 2009;
315 McConnell et al., 2010; Kim et al., 2011; Klaver et al., 2011). Optical calculations were computed
316 over the spectral range of the WELAS using Mie theory for spherical particles by fixing n at 1.47, 1.50
317 and 1.53, and by varying k in steps of 0.001 between 0.001 and 0.005. The spectrum of the WELAS
318 lamp needed for optical calculations was measured in the laboratory (Fig. S2, supplementary material).
319 D_g was then set at the mean ± one standard deviation of the values obtained for the different n and k.
320 After calculations, the WELAS D_g range became 0.65-73.0 µm with an associated uncertainty of <5%
321 for D_g<10 µm and between 5 and 7% at larger diameters. A very low counting efficiency was observed
322 for the WELAS below 1 µm, thus data in this size range were discarded.

323 For the SkyGrimm, the D_{opt} to D_g diameter conversion was performed with a procedure similar to that
324 used for the WELAS. After calculations, the D_g range for the SkyGrimm became 0.29-68.2 µm with
325 an associated uncertainty <15.2% at all diameters. The inter-calibration between the SkyGrimm and
326 the master instrument showed ~~a~~ relatively good agreement (<20% difference in particle number) at

327 D_g<1 μm, but a large disagreement (up to 300% difference) at D_g>1 μm. Based on inter-comparison

328 data, a recalibration curve was calculated for the SkyGrimm in the range D_g<1 μm, and the data for

329 D_g>1 μm were discarded. The SkyGrimm particle concentration was also corrected for the flow rate of

330 the instrument, which during the experiment was observed to vary between 0.7 and 1.2 L min^{-1} com-

331 pared to its nominal value at 1.2 L min^{-1}.

332

333 **2.3.2 Correction for particle losses in sampling lines and determination of the full dust size dis-**

334 **tribution at the input of each instrument**

335 In order to compare and combine extractive measurements (size distribution, filter sampling, and SW

336 optics), particle losses due to aspiration and transmission in the sampling lines were calculated using

337 the Particle Loss Calculator (PLC) software (von der Weiden et al., 2009). Inputs to the software in-

338 clude the geometry of the sampling line, the sampling flow rate, the particle shape factor χ, and the

339 particle density (set at 2.5 g cm^{-3} for dust).

340 Particle losses for the instruments measuring the number size distribution (SMPS, WELAS, and

341 SkyGrimm) were calculated. This allowed reconstructing the dust size distribution suspended in the

342 CESAM chamber that corresponds to the size distribution sensed by the FTIR and that is needed for

343 optical calculations in the LW. Particle loss was found negligible at D_g<1 μm, reaching 50% at D_g~5

344 μm, 75% at D_g ~6.3 μm, and 95% at D_g ~8 μm for the WELAS, the only instrument considered in the

345 super-micron range. Data for the WELAS were then corrected as

346
$$\left[dN / d\log D_g \right]_{Corr,WELAS} = \left[dN / d\log D_g \right]_{WELAS} / \left[1 - L_{WELAS}\left(D_g \right) \right] \quad (3)$$

347 where [dN/dlogD$_g$]$_{WELAS}$ is the size measured by the WELAS and $L_{WELAS}(D_g)$ is the calculated particle

348 loss as a function of the particle diameter. Data at D_g>8 μm, for which the loss is higher than 95%,

349 were excluded from the dataset due to their large uncertainty. The uncertainty on $L_{WELAS}(D_g)$ was es-

350 timated with a sensitivity study by varying the PLC software values of the input parameters within

351 their ~~error bars~~uncertainties. The $L_{WELAS}(D_g)$ uncertainty varies between ~50% at 2 μm to ~10% at 8

352 μm. The total uncertainty in the WELAS-corrected size distribution was estimated as the combination

353 of the dN/dlogD$_g$ standard deviation on the 10-min average and the $L_{WELAS}(D_g)$ uncertainty.

12

354 The full size distribution of dust aerosols within the CESAM chamber $\left[dN/d\log D_g\right]_{CESAM}$ was deter-

355 mined by combining SMPS and SkyGrimm data with WELAS loss-corrected data: the SMPS was tak-

356 en at $D_g<0.3$ µm, the SkyGrimm at $D_g=0.3\text{-}1.0$ µm, and the WELAS at $D_g=1.0\text{-}8.0$ µm. Data were then

357 interpolated in steps of $d\log D_g=0.05$. An example of the size distributions measured by the different

358 instruments is shown in Fig. S3 in the supplement for this paper. Above 8 µm, where WELAS data

359 were not available, the dust size distribution was extrapolated by applying a single-mode lognormal fit.

360 The fit was set to reproduce the shape of the WELAS distribution between $D_g\sim3\text{-}4$ and 8 µm.

361 Particle losses in the filter sampling system ($L_{filter}(D_g)$) were calculated estimating the size-dependent

362 particles losses that would be experienced by an aerosol with the size distribution in CESAM recon-

363 structed from the previous calculations. Losses for the sampling filter were negligible for $D_g<1$ µm,

364 and increased to 50% at $D_g\sim6.5$ µm, 75% at $D_g\sim9$ µm, and 95% at $D_g\sim12$ µm. The loss function,

365 $L_{filter}(D_g)$, was used to estimate the dust size distribution at the input of the filter sampling system as

366
$$\left[dN/d\log D_g\right]_{filter}=\left[dN/d\log D_g\right]_{CESAM}*\left[1-L_{filter}\left(D_g\right)\right] \quad (4).$$

367 As a consequence of losses, the FTIR and the filters sense particles over different size ranges. Figure

368 S4 (supplementary material) illustrates this point by showing a comparison of between the calculated

369 size distribution within CESAM and that sampled on filters for one typical case. An underestimation of

370 the particle number on the sampling filter compared to that measured in CESAM is observed above 10

371 µm diameter. While the filter samples would underestimate the mass concentration in the chamber, the

372 relative proportions of the main minerals should be well represented. As a matter of fact, at emission,

373 where particles of diameters above 10 µm are most relevant, the mineralogical composition in the 10-

374 20 µm size class matches that of particles of diameters between 5 and 10 µm (Kandler et al., 2009).

375 When averaging, and also taking into account the contribution of the mass of the 10-20 µm size class

376 to the total, differences in the relative proportions of minerals do not exceed 10%.

377

378

379 **2.4 Analysis of the mineralogical composition of the dust aerosol mineralogical composition**

380 The mineralogical composition of the aerosol particles collected on the filters was determined by com-

381 bining: X-Ray Diffraction (XRD, Panalytical model Empyrean diffractometer) to estimate the parti-

382 cles' mineralogical composition in terms of clays, quartz, calcite, dolomite, gypsum, and feldspars;

13

Wavelength Dispersive X-ray Fluorescence (WD-SFX, Panalytical PW-2404 spectrometer) to determine the dust elemental composition (Na, Mg, Al, Si, P, K, Ca, Ti, Fe) (±8-10% uncertainty); and X-ray Absorption Near-Edge Structure (XANES) ~~a~~ to retrieve the content of iron oxides (±15% on the mass fraction) and their speciation between hematite and goethite~~nalysis~~. Half of the ~~nuclepore~~Nuclepore filters were analyzed by XRD and the other half by WD-SFX and XANES. Full details on the WD-SFX and XANES measurements and data analysis are provided elsewhere (Caponi et al., in preparation). Here we describe the XRD measurements.

XRD analysis was performed using a Panalytical model Empyrean diffractometer with Ni-filtered CuK$_\alpha$ radiation at 45 kV and 40 mA. Samples were scanned from 5 to 60° (2θ) in steps of 0.026°, with a time per step of 200 s. Samples were prepared and analyzed according to the protocols of Caquineau et al. (1997) for low mass loadings (load deposited on filter <800 μg). Particles were first extracted from the filter with ethanol, then concentrated by centrifuging (25,000 rpm for 30 min), diluted with deionized water (pH ~ 7.1), and finally deposited on a pure silicon slide.

For well-crystallized minerals, such as quartz, calcite, dolomite, gypsum, and feldspars (orthoclase, albite), a mass calibration was performed in order to establish the relationship between the intensity of the diffraction peak and the mass concentration in the aerosol samples, according to the procedure described in Klaver et al. (2011). The calibration coefficients K_i, representing the ratio between the total peak surface area in the diffraction spectra (S_i) and the mass m_i of the ith-mineral, are reported in Table S1 in the supplementary material. The error in the obtained mass of each mineral was estimated with the error propagation formula taking into account the uncertainty in S_i and the calibration coefficients K_i. The obtained uncertainty is ±9% for quartz, ±14% for orthoclase, ±8% for albite, ±11% for calcite, ±10% for dolomite, and ±18% for gypsum.

Conversely, the mass concentration of clays (kaolinite, illite, smectite, palygorskite, chlorite), also detected in the samples, cannot be quantified in absolute terms from the XRD spectra due to the absence of appropriate calibration standards for these components (Formenti et al., 2014). Hence, the total clay mass was estimated as the difference between the total dust mass ~~calculated from particle size distribution $\left[dN/d\log D_g \right]_{filter}$~~ and the total mass of quartz, calcium-rich species, and ~~and~~ feldspars, estimated after XRD calibration, and iron oxides, estimated from XANES ~~estimated after calibration~~. The mass of organic material was neglected in the calculation: ~~,~~ its~~as well as that of iron and titanium oxides, whose~~ contributions, however, should not exceed ~~5~~3% according to the literature (Lepple and

413 Brine, 1976~~; Lafon et al., 2006; Formenti et al., 2014~~). The total dust mass was calculated in two ways:
414 ~~calculated~~ from the particle size distribution $\left[dN / d\log D_g \right]_{filter}$ (M_{size}, by assuming a dust density of 2.5

Mis en forme : Anglais (États Unis), Indice

415 g cm^{-3}) and from the estimated elemental composition ($M_{elemental}$, as described in Caponi et al., submit-
416 ted). Our results show that M_{size} systematically overestimates $M_{elemental}$. As a result, using M_{size} or M_{el-}
417 $_{emental}$ would result in different clay mass fractions. In the absence of a way to ~~estimate~~assess whether
418 ~~which between~~ M_{size} ~~or~~and $M_{elemental}$ is ~~the correct one~~more accurate, we decided to estimate the clays
419 mass for each dust sample as the mean ± maximum variability of the values obtained by using the two
420 mass estimates, M_{size} and $M_{elemental}$. This approach ~~would~~should give a reasonable approximation of the
421 average clay content in the dust samples. The error in the obtained clay mass varies in the range 14–
422 100%.

423 ~~Then~~Subsequently, the mass fraction for each mineral was estimated as the ratio of the mass of the
424 ~~considered~~ mineral divided by the total mass of all minerals.

425 For the Northern African and Eastern Asian aerosols only, the mass apportionment between the differ-
426 ent clay species was based on literature values of illite-to-kaolinite (I/K) and chlorite-to-kaolinite
427 (Ch/I) mass ratios (Scheuvens et al., 2013; Formenti et al. 2014). For the other samples, only the total
428 clay mass was estimated.
429

430 **3. Retrieval of the LW complex refractive ind~~ex~~ices**

431 An optical inversion procedure was applied to retrieve the LW complex refractive index (m=n–ik) of
432 the dust aerosols based on the simultaneous measurements of the particle LW spectra and size. Starting
433 from the number size distribution, $\left[dN / d\log D_g \right]_{CESAM}$, the LW absorption coefficient, $\beta_{abs}(\lambda)$, meas-
434 ured in CESAM can be calculated as:

$$\left(\beta_{abs}(\lambda) \right)_{calc} = \sum_{D_g} \frac{\pi D_g^2}{4} Q_{abs}\left(m, \lambda, D_g \right) \left[\frac{dN}{d\log D_g} \right]_{CESAM} d\log D_g \qquad (5)$$

436 where $Q_{abs}(m,\lambda,D_g)$ is the particle absorption efficiency and $\frac{\pi D_g^2}{4} \left[\frac{dN}{d\log D_g} \right]_{CESAM}$ is the surface size dis-

Code de champ modifié

437 tribution of the particles. As the simplest approach, Q_{abs} can be computed using Mie theory for spheri-
438 cal particles.

439   Our retrieval algorithm consists of iteratively varying m in expression (5) until $(\beta_{abs}(\lambda))_{calc}$ matches the

440   measured $\beta_{abs}(\lambda)$. However, as m is a complex number with two variables, an additional condition is

441   needed. According to electromagnetic theory, n and k must satisfy the Kramers-Kronig (K-K) relation-

442   ship (Bohren and Huffmann, 1983):

$$n(\omega) - 1 = \frac{2}{\pi} P \int_0^\infty \frac{\Omega \cdot k(\Omega)}{\Omega^2 - \omega^2} \cdot d\Omega \quad (6)$$

443

444   with ω the angular frequency of radiation ($\omega = 2\pi c/\lambda$, [s^{-1}]), and P the principal value of the Cauchy in-

445   tegral. Equation (6) means that if $k(\lambda)$ is known, then $n(\lambda)$ can be calculated accordingly. Hence, the K-

446   K relation is the additional condition besides (5) to retrieve n and k. A direct calculation of the K-K

447   integral is, however, very difficult as it requires the knowledge of k over an infinite wavelength range.

448   A useful formulation, which permits one to obtain the couple of n-k values that automatically satisfy

449   the K-K condition, is the one based on the Lorentz dispersion theory. In the Lorentz formulation, n and

450   k may be written as a function of the real (ε_r) and imaginary (ε_i) parts of the particle dielectric function

451   ~~as~~:

$$n(\omega) = \left(\frac{1}{2} \left[\sqrt{(\varepsilon_r(\omega))^2 + (\varepsilon_i(\omega))^2} + \varepsilon_r(\omega) \right] \right)^{1/2} \quad (7a)$$

452

$$k(\omega) = \left(\frac{1}{2} \left[\sqrt{(\varepsilon_r(\omega))^2 + (\varepsilon_i(\omega))^2} - \varepsilon_r(\omega) \right] \right)^{1/2} \quad (7b)$$

453

454      $\varepsilon_r(\omega)$ and $\varepsilon_i(\omega)$ can be in turn expressed as the sum of N Lorentzian harmonic oscillators:

$$\varepsilon_r(\omega) = \varepsilon_\infty + \left[\sum_{j=1}^{N} \frac{F_j\left(\omega_j^2 - \omega^2\right)}{\left(\omega_j^2 - \omega^2\right)^2 + \gamma_j^2 \omega^2} \right] \quad (8a)$$

455

$$\varepsilon_i(\omega) = \sum_{j=1}^{N} \frac{F_j \gamma_j \omega}{\left(\omega_j^2 - \omega^2\right)^2 + \gamma_j^2 \omega^2} \quad (8b)$$

456

457   where $\varepsilon_\infty = n_{vis}^2$ is the real dielectric function in the limit of visible wavelengths, ~~and~~ n_{vis} the real part

458   of the refractive index in the visible, and (ω_j, γ_j, F_j) are the three parameters (eigenfrequency, damping

459   factor, and strength) characterizing the j-th oscillator.

16

460   In our algorithm we combined (7a)-(7b) and (8a)-(8b) with (5) to retrieve n-k values that allow both to

461   reproduce the measured $\beta_{abs}(\lambda)$ and to satisfy the K-K relationship. In practice, in the iteration proce-

462   dure only one of the two components of the refractive index (in our case, k) was varied, while the other

463   (n) was recalculated at each step based on the values of the oscillator parameters (ω_j, γ_j, F_j) obtained

464   from a best fit for k. In the calculations, the initial value of $k(\lambda)$ was set at $k(\lambda)=\lambda\beta_{abs}(\lambda)/4\pi$, then in the

465   iteration procedure, $k(\lambda)$ was varied in steps of 0.001 without imposing any constraint on its spectral

466   shape. Initial values of the (ω_j, γ_j, F_j) parameters were set manually set based on the initial spectrum of

467    $k(\lambda)$. Between 6 and 10 oscillators were needed to model the $k(\lambda)$ spectrum for the different cases. The

468   fit between $k(\lambda)$ and Eq. (7b) was performed using the Levenberg-Marquardt technique. The iteration

469   procedure was stopped when the condition: $|(\beta_{abs}(\lambda))_{calc} - \beta_{abs}(\lambda)|<1\%$ is was met at all wavelengths.

470   Optical calculations were performed between 6 and 16 μm, within a range where FTIR- measured

471   scattering could be neglected (see Sect. 2.2). The uncertainties caused by this choice are discussed in

472   Sect. 3.1. Below 6 μm, $k(\lambda)$ was then fixed to the value obtained at 6 μm. Calculations were performed

473   over 10-min intervals.

474   For each experiment and for each 10-min interval, the value of n_{vis} to use in Eq. (8a) was obtained

475   from optical calculations using the simultaneous measurements of the SW scattering and absorption

476   coefficients performed in CESAM (Di Biagio et al., in preparation). For the various aerosol samples

477   considered here, the value of n_{vis} varied between 1.47 and 1.52 with an uncertainty <2%. This ap-

478   proach is better than the one used in DB14, where the value of n_{vis} was manually adjusted for succes-

479   sive trials. Specifically, in DB14, n_{vis} was varied and set to the value that allowed best reproducing the

480   measured dust scattering signal below 6 μm. As discussed in Sect. 2.2, however, only a fraction of the

481   total dust scattering is measured by the FTIR. As a result, the n_{vis} values obtained in DB14 were con-

482   siderably lower thant the values generally assumed for dust (n_{vis} =1.32-1.35 compared to 1.47-1.53

483   from the literature;, e.g., Osborne et al., 2008; McConnell et al., 2010), with a possible resulting over-

484   all underestimation of n. Here, instead, the n_{vis} value was obtained based on additional SW optical

485   measurements, which ensured a more reliable estimate of the whole spectral n.

486   The validity of the proposed retrieval procedure was assessed by performing a control experiment

487   where ammonium sulfate aerosols were injected in the chamber. Ammonium sulfate has been widely

488   studied in the past and its optical properties are well known (e.g., Toon et al., 1976; Flores et al.,

489   2009). The description and the results of the control experiment are reported in Appendix 1.

17

490

3.1 Caveats on the retrieval procedure for the LW refractive index

The procedure for the retrieval of the complex refractive index presented in the previous section combines optical calculations, the Kramers-Kronig relation, and the Lorentz dispersion theory, and was based on measurements of spectral absorption and particle size distribution. The approach is quite sensitive to the accuracy and representativeness of the measurements and assumptions in the optical calculations. We now list the different points that need to be addressed to insure the accuracy of the retrieval procedure.

1. First, our optical calculations (Eq. (5)) use Mie theory for spherical particles. This is expected to introduce some degrees of uncertainties in simulated LW spectra, especially near the resonant peaks (Legrand et al., 2014). However, as discussed in Kalashnikova and Sokolik (2004), deviations from the spherical behaviourbehavior are mostly due to the scattering component of extinction since irregularly-shaped particles have larger scattering efficiencies than spheres. In contrast, particle absorption is much less sensitive to particle shape. Given that our measured spectra are dominated by absorption, we can therefore reasonably assume that Mie theory is well suited to model our optical data. It also has also to be pointed out that at present almost all climate models use Mie theory to calculate dust optical properties. So, with the aim of implementing our retrieved refractive indices in model schemes, it is required that the same optical assumptions are done in the twoboth cases, i.e., the optical theory used in models and that used for refractive index retrieval.

2. Second, as discussed in Sect. 2.2, measured dust spectra at wavelengths > 6 μm represent only dust absorption, with minimal contribution from scattering. Dufresne et al. (2002) show that the contribution of LW scattering from dust is quite important in the atmosphere, especially under cloudy conditions. Therefore, the impact of neglecting the scattering contribution has to be assessed. The retrieval procedure used in this study is nearly independent of whether dust extinction or only absorption only is used. Indeed, the combination of Eq. (5) with the Lorentz formulation in Eq. (7a) and (7b) ensures the retrieval of n-k couples that are theoretically correct (fulfilling the K-K relationship), and the specific quantity to reproduce by Eq. (5) – i.e., extinction or absorption – provides only a mathematical constraint on the retrieval. Therefore, neglecting the scattering contribution to the LW spectra has no influence on the estimates of the refractive index, and the real and the imagi-

519 nary parts obtained in this study represent both the scattering and the absorption components of the
520 dust extinction.

521 3. Third, <u>our</u> optical calculations are performed only at wavelengths > 6 μm, while in the range 2-6 μm
522 $k(\lambda)$ is fixed to the value obtained at 6 μm. We examine the accuracy of this assumption. Given that,
523 over the whole 2-6 μm range, dust is expected to have a negligible absorption (k is close to zero, see
524 Di Biagio et al., 2014a), fixing k at the value at 6 μm is a reasonable approximation. Concerning the
525 impact of this assumption on the retrieval of n, it should be pointed out that in the range 2-6 μm,
526 where~~n~~ k is very low, the shape of the n spectrum is determined only by the anchor point n_{vis}, and
527 the exact value of k is not relevant.

528

529 **3.2 Uncertainty estimation**

530 The uncertainty in the retrieved refractive index was estimated with a sensitivity analysis. Towards this
531 goal, n and k were also obtained by using as input to the retrieval algorithm the measured $\beta_{abs}(\lambda)$ and
532 size distribution ± their estimated uncertainties. The <u>differences between the</u>~~deviations of the values of~~
533 <u>so obtained</u> n and k <u>and the n and k</u> ~~retrieved in the sensitivity study with respect to those obtained~~
534 ~~in~~<u>from</u> the <u>first</u>~~first~~ inversion w~~ere~~<u>ere</u> estimated. Then, we computed a quadratic combination of these
535 different factors to deduce the uncertainty in n and k.

536 The results of the sensitivity study indicated that the measurement uncertainties on $\beta_{abs}(\lambda)$ (±10%) and
537 the size distribution (absolute uncertainty on the number concentration, ±20-70%<u>, with values larger</u>
538 <u>than 30% found for diameters between about 0.5 and 2.0 μm</u>) have an impact of ~10-20% on the re-
539 trieval of n and k.

540 Additionally, a sensitivity analysis was performed to test the dependence of the retrieved LW refrac-
541 tive index on the accuracy of the shape of the size distribution above 8 μm. As discussed in Sect. 2.3.2,
542 the size distribution $\left[dN/d\log D_g\right]_{CESAM}$ used for the optical calculations was measured between 0.1 and
543 8 μm based on SMPS, SkyGrimm, and WELAS data. However, it was extrapolated to larger sizes by
544 applying a lognormal mode fit for particle diameters >8 μm, where measurements were not available.
545 The extrapolation was set to reproduce the shape of the WELAS size distribution between D_g~3-4 and
546 8 μm. In the sensitivity study, n and k were also obtained by using two different size distributions as
547 input to the retrieval algorithm, in which the extrapolation curve at D_g>8μm was calculated by consid-

19

548 ering the WELAS data ± their estimated y-uncertainties. The results of the sensitivity study indicate

549 that a change of the extrapolation curve between its minimum and maximum may induce a variation of

550 less than 10% on the retrieved n and k.

551 The total uncertainty ~~i~~on n and k, estimated as the quadratic combination of these factors, was close to

552 20%.

553 An additional source of uncertainty linked to the size distribution, which however we do not quantify

554 here, concerns the choice of performing a single-mode extrapolation above 8 μm, which means ne-

555 glecting the possible presence of larger dust modes.

556

557 **4. Selection of soil samples: representation of the dust mineralogical variability at the global**

558 **scale**

559 Nineteen soil samples were selected for experiments from a collection of 137 soils from various source

560 areas worldwide. Their location is shown in Fig. 2. The main information on the provenance of the

561 selected soils is summarized in Table 2. Soils were grouped in the nine regions identified by Ginoux et

562 al. (2012): Northern Africa, Sahel, Eastern Africa and Middle East, Central Asia, Eastern Asia, North

563 America, South America, Southern Africa, and Australia. The choice of the soils to analyze was per-

564 formed according to two criteria: 1) soils had to represent all major arid and semi-arid regions, as de-

565 picted by Ginoux et al. (2012) and 2) their mineralogy should envelope the largest possible variability

566 of the soil mineralogical composition at the global scale.

567 A large set of soils were available for Northern Africa, the Sahel, Eastern Africa and the Middle East,

568 Eastern Asia, and Southern Africa. Here, the selection was performed using as guidance the global

569 database of Journet et al. (2014), reporting the composition of the clay (<2 μm diameter) and silt (<60

570 μm diameter) fractions in terms of 12 different minerals. Amongst them, we analyzed the variability of

571 the minerals that are most abundant in dust as well as most optically relevant to LW absorption, name-

572 ly, illite, kaolinite, calcite, and quartz in the clay fraction, and calcite and quartz in the silt fraction. The

573 comparison of the ~~extracted (from the Journet database)~~ clay and silt compositions of the soils extract-

574 ed from the Journet database with~~corresponding to~~ the available samples resulted in the selection of

575 five samples for Northern Sahara, three for the Sahel, three for Eastern Africa and the Middle East, and

576 two for Eastern Asia and Southern Africa, as listed in Table 2. These soils constitute fifteen of the

577 nineteen samples used in the experiments. More information on these soils is provided in the follow-
578 ing.

579 For Northern Africa, we selected soils from the Northern Sahara (Tunisia, Morocco), richer in calcite
580 and illite, Central Sahara (Libya and Algeria), enriched in kaolinite compared to illite and poor in cal-
581 cite, and Western Sahara (Mauritania), richer in kaolinite. The three samples from the Sahel are from
582 Niger, Mali and Chad (sediment from the Bodélé depression), and are enriched in quartz compared to
583 Saharan samples. The selected soils from Northern Africa and the Sahel represent important sources
584 for medium and long-range dust transport towards the Mediterranean (Israelevich et al., 2002) and the
585 Atlantic Ocean (Prospero et al., 2002; Reid et al., 2003). In particular, the Bodélé depression is one of
586 the most active sources at the global scale (Goudie and Middleton, 2001; Washington et al., 2003).

587 The three soils from Eastern Africa and the Middle East are from Ethiopia, Saudi Arabia, and Kuwait,
588 which are important sources of dust in the Red and the Arabian seas (Prospero et al., 2002) and the
589 North Indian Ocean (Leon and Legrand, 2003). These three samples differ in their content of calcite,
590 quartz, and illite-to-kaolinite mass ratio (I/K).

591 For the second largest global source of dust, Eastern Asia, we considered two samples representative
592 of the Gobi and the Taklimakan deserts, respectively. These soils differ in their content of calcite and
593 quartz. Unfortunately, no soils are available for Central Asia, mostly due to the difficulty of sampling
594 these remote desert areas.

595 For Southern Africa, we selected two soils from the Namib desert, one soil from the area between the
596 Kuiseb and Ugab valleys (Namib-1) and one soil from the Damaraland rocky area (Namib-2), both
597 sources of dust transported towards the South-Eastern Atlantic (Vickery et al. 2013). These two soils
598 present different compositions in term of calcite content and I/K ratio.

599 ~~Differently from~~In contrast to Africa, the Middle East, and Eastern Asia, ~~Aa~~ -very limited number of
600 samples were available in the soil collection for North and South America and Australia. Four of the
601 nineteen soils used in our experiments were taken from these regions. These soils were collected in the
602 Sonoran Desert for North America, in the Atacama and Patagonian deserts for South America, and in
603 the Strzelecki desert for Australia. The Sonoran Desert is a permanent source of dust in North Ameri-
604 ca, the Atacama desert is the most important source of dust in South America, whilst Patagonia emis-
605 sions are relevant for long-range transport towards Antarctica (Ginoux et al., 2012). The Strzelecki
606 desert is the seventh largest desert of Australia. No mineralogical criteria were applied to these areas.

607 A summary of the mineralogical composition of the nineteen selected soils is shown in Fig. 3 in com-

608 parison with the full range of variability obtained considering the full data from the different nine dust

609 source areas. As illustrated by this figure, the samples chosen for this study cover the entire global

610 variability of the soil compositions derived by Journet et al. (2014).

611

612 **5. Results**

613 **5.1 Atmospheric representativity: mineralogical composition**

614 The mineralogical composition measured for~~of~~ the nineteen ~~generated~~ aerosol samples ~~as measured by~~

615 ~~XRD analysis~~ is shown in Fig. 4. Data on the full mineralogy, also including the minimum and the

616 maximum of the estimated dust clay content, are provided in Table S2 in the supporting material ~~of~~

617 ~~this manuscript.~~ The aerosol composition is dominated by clays (~~~55~~46-92~~5~~% for the different sam-

618 ples), with variable contents of quartz, calcite, dolomite, and feldspars. Identified clay species are: il-

619 lite, kaolinite, smectite, palygorskite, and chlorite. Illite and kaolinite are ubiquitous; smectite and

620 palygorskite are detected in some of the samples (Algeria, Ethiopia, Saudi Arabia, Kuwait, Arizona,

621 and both samples from Namibia); in contrast, chlorite is found only in the two Chinese and in the Chil-

622 ean samples. The estimated contribution of illite, kaolinite and chlorite to the total clay mass are shown

623 in Fig. 4 for Northern Africa (Algerian sample excluded, given that also smectite is detected in this

624 sample) and Eastern Asian aerosols. Quartz ranges from ~~2~~3 to 34~~2~~% by mass in the samples, with the

625 highest values measured for Patagonia, Niger, Australia, Mali, and Bodélé~~Patagonia, and Niger~~ dust.

626 Calcite is less than ~~17~~23%, with maxima observed for Tunisia, Morocco, and Gobi dusts. Conversely,

627 only minor traces of dolomite (<~~2~~3%) are detected in all the different samples. Finally, feldspars (or-

628 thoclase and albite) represent less than ~~9~~15% of the dust composition.

629 The ~~O~~observations from the present study capture well the global tendencies of the dust mineralogical

630 compositions as observed in several studies based on aerosol field observations, both from ground-

631 based and airborne samples (e.g., Sokolik and Toon, 1999; Caquineau et al., 2002; Shen et al., 2005 ;

632 Jeong, 2008; Kandler et al., 2009; Scheuvens et al., 2013; Formenti et al., 2014). For instance, at the

633 scale of Northern Africa, we correctly reproduce the geographical distribution of calcite, which is ex-

634 pected to be larger in Northern Saharan samples (Tunisia, Morocco), and very low or absent when

635 moving towards the Southern part of the Sahara and the Sahel (Libya, Algeria, Mauritania, Niger, Ma-

636 li, and Bodélé ~~samples~~). Similarly, we observe an increase of the aerosol quartz content from Northern

22

Sahara towards the Sahel, which is well known at the regional scale of Northern Africa (e.g., Caquineau et al., 2002). Also, we identify the presence of chlorite in the Eastern Asian samples (Gobi and Taklimakan), in agreement with field observations in this region (Shen et al., 2005). A more direct comparison of our data with field measurements of the dust mineralogical composition is rather complicated due to possible differences linked to the size distribution and representativeness of the specific sources between our data and field measurements (Perlwitz et al., 2015a, 2015b). For the Niger sample only, however, a semi-quantitative comparison can be performed against field data of the dust mineralogy obtained for aerosols collected at Banizoumbou during the AMMA (African Monsoon Multidisciplinary Analysis) campaign in 2006. The mineralogy for these samples was provided by Formenti et al. (2014). For a case of intense local erosion at Banizoumbou, they showed that the aerosol is composed of 51% (by volume) of clays, 41% of quartz, and 3% of feldspars. Our Niger sample generated from the soil collected at Banizoumbou, is composed of 6451% (±5.1%) (by mass) of clays, 307% (±3%) of quartz, and 56% (±0.8%) of feldspars, in relativevery good agreement with the field observations.

5.2 Atmospheric representativity: size distribution

The size distribution of the dust aerosols measured at the peak of the dust injection in the chamber is shown in Fig. 5. We report in the plot the normalized surface size distribution, defined as:

$$\frac{dS}{d\log D_g}(\text{normalized}) = \frac{1}{S_{tot}} \cdot \left(\frac{\pi}{4} D_g^2 \left[dN/d\log D_g \right]_{CESAM} \right) \qquad (9)$$

with S_{tot} the total surface area. The surface size distribution is the quantity that determines dust optical properties (see Eq. 5). The dust surface size distributions present multimodal structures, where the relative proportions of the different modes vary significantly between the samples. The dust mass concentration at the peak of the injection estimated from size distribution data varies between 2 and 310 mg m^{-3}. These values are comparable to what has been observed close to sources in proximity to dust storms (Goudie and Middleton, 2006; Rajot et al., 2008; Kandler et al., 2009; Marticorena et al., 2010). Given that the protocol used for soil preparation and aerosol generation is always the same for the different experiments, the observed differences in both the shape of the size distribution and the mass concentration of the generated dust aerosols are attributableed to the specific characteristics of the soils, which may be more or less prone to produce coarse-size particles.

23

666 The comparison of the chamber data with observations of the dust size distribution from several air-
667 borne campaigns in Africa and Asia is shown in Fig. 6. This comparison suggests that the shape of the
668 size distribution in the chamber at the peak of the injection accurately mimics the dust distribution in
669 the atmosphere near sources.

670 The time evolution of the normalized surface size distribution within CESAM is shown in Fig. 7 for
671 two examples taken from the Algeria and Atacama experiments, while an example of the dust number
672 and mass concentration evolution over an entire experiment is illustrated in Fig. S5 (supplementary
673 material). The Algeria and Atacama samples were chosen as representative of different geographic areas and
674 different concentration levels in the chamber. As shown in Fig. 7, the dust size distribution strongly
675 changes with time due to gravitational settling: the coarse mode above 5 μm rapidly decreases, due to
676 the larger fall speed at these sizes (~1 cm s^{-1} at 10 μm, compared to ~0.01 cm s^{-1} at 1 μm; Seinfeld and
677 Pandis, 2006), and the relative importance of the fraction smaller than D_g=5 μm increases concurrent-
678 ly. In the chamber we are thus able to reproduce very rapidly (about 2 hours) the size-selective gravita-
679 tional settling, a process that in the atmosphere may takes about one to five days to occur (Maring et
680 al., 2003). In order to compare the dust gravitational settling in the chamber with that observed in the
681 atmosphere the following analysis was performed. For both Algeria and Atacama soils, the fraction of
682 particles remaining in suspension in the chamber as a function of time versus particle size was calcu-
683 lated as $dN_i(D_g)/dN_0(D_g)$, where $dN_i(D_g)$ is the number of particles measured by size class at the i time
684 i (i corresponding to 30, 60, 90 and 120 min after injection) and $dN_0(D_g)$ represents the size-dependent
685 particle number at the peak of the injection. The results of these calculations are shown in the lower
686 panels of Fig. 7, where they are compared to the fraction remaining airborne after 1-2 days obtained in
687 the field study by Ryder et al. (2013b) for mineral dust transported out of Northern Africa in the Sa-
688 haran Air Layer (Karyampudi et al., 1999), that is, at altitudes between 1.5 and 6 km above sea level.
689 The comparison indicates that the remaining particle fraction observed 30 minutes after the peak of the
690 injection is comparable to that obtained by Ryder et al. (2013b) for particles between ~0.4 and 3 μm
691 for the Algeria case, and ~0.4 and 8 μm for the Atacama casesmaller than ~3 to 8 μm (depending on
692 the soil), but that the depletion is much faster for both smaller and larger particles. This suggests, on
693 the one hand, that the number fraction of coarse particles in the chamber depends on the initial size
694 distribution, that is, on the nature of the soil itself. On the other hand, it shows the limitation of the
695 four-blade fan in providing a vertical updraft sufficient to counterbalance the gravimetric deposition
696 for particles larger than about 8 μm. This point, however, is not surprising since it is clear that in the

24

697 laboratory it is not possible to reproduce the wide range of dynamical processes that occur in the real
698 atmosphere, and so to obtain a faithful reproduction of dust gravitational settling and the counteracting
699 re-suspension mechanisms. Nonetheless, it should be noted that the rate of removal is higher at the
700 earlier stages of the experiments than towards their end. The size-dependent particle lifetime, defined
701 as the value at which dN/dN_0 is equal to $1/e$ (McMurry and Rader, 1985), is relatively invariant for
702 particles smaller than $D_g < \sim 2$ μm (> 60 min). This indicates that no significant distortion of the parti-
703 cle size distribution occurs after the most significant removal at the beginning of the experiment, and
704 that the fine-to-coarse proportions are modified with time in a manner consistent with previous field
705 observations on medium- to long-transport (e.g., Maring et al., 2003; Rajot et al., 2008; Reid et al.,
706 2008; Ryder et al., 2013b; Denjean et al., 2016).

707

708 **5.3 Dust LW extinction and complex refractive index spectra for the different source regions**

709 Figure 8 shows the dust LW spectral extinction coefficients measured at the peak of the injection for
710 the nineteen aerosol samples. As discussed in Sect. 2.2, the spectra in Fig. 8 show the contribution of
711 dust scattering below 6 μm, while the absorption spectrum only is measured above 6 μm. In this wave-
712 length range, significant differences are observed when comparing the samples, which in turn are
713 linked to differences in their mineralogical composition.

714 Figure 8 allows the identification of the spectral features of the minerals presenting the strongest ab-
715 sorption bands, in particular in the 8-12 μm atmospheric window (Table 3). The most prominent ab-
716 sorption peak is found around 9.6 μm for all samples, where clays have their Si—O stretch resonance
717 peak. The shape around the peak differs according to the relative proportions of illite and kaolinite in
718 the samples, as is illustrated with the results for the Tunisia, Morocco, Ethiopia, Kuwait, Arizona, Pat-
719 agonia, Gobi, and Taklimakan samples (richer in illite) compared to the Libya, Algeria, Mauritania,
720 Niger, Bodélé, Saudi Arabia, and Australia samples (richer in kaolinite). Aerosols rich in kaolinite also
721 show a secondary peak at ~10.9 μm. The spectral signature of quartz at 9.2 and 12.5-12.9 μm is ubiq-
722 uitous, with a stronger contribution in the Bodélé, Niger, Patagonia, and Australia samples. Aerosols
723 rich in calcite, such as the Tunisia, Morocco, Saudi Arabia, Taklimakan, Arizona, Atacama, and Na-
724 mib-1 samples show absorption bands at ~7 and 11.4 μm. Conversely, these are not present in the oth-
725 er samples and in particular in none of the samples from the Sahel. Finally, the contribution of feld-
726 spars (albite) at 8.7 μm is clearly detected only for the Namib-1 sample.

25

727 The intensity of the absorption bands depend strongly on the particle size distribution, in particular on
728 the contribution of the aerosol super-micron fraction, as well as on the total dust mass concentration.
729 These, as discussed in the previous section, are associated with the specific characteristics of each of
730 the soils used and their propensity for dust emission. The highest values of dust absorption that can be
731 seen in Fig. 8 for the 8–12 μm spectral region appear for the Bodélé aerosol sample. In this particular
732 sample, the super-micron particles represent 45% of the total particle number at the peak of the injec-
733 tion, and this sample showed the highest mass concentration in the chamber (310 mg m^{-3}). Conversely,
734 the lowest absorption is measured for the aerosols from Mauritania, Mali, Kuwait, and Gobi, for which
735 the super-micron particle fraction and the mass concentrations are lower.

736 The intensity of the spectral extinction rapidly decreases after injection, following the decrease of the
737 super-micron particle number and mass concentration. As an example, Fig. 9 shows the temporal evo-
738 lution of the measured extinction spectrum for the Algeria and Atacama aerosols. The intensity of the
739 absorption band at 9.6 μm is about halved after 30 min and reduced to ~20-30% and <10% of its initial
740 value after 60 min and 90-120 min, respectively. Because of the size-dependence of the mineralogical
741 composition, notably the relative proportions of quartz and calcite with respect to clays (Pye et al.,
742 1987), settling could also modify the spectral shape of the extinction spectrum. This effect was inves-
743 tigated for the two example cases, Algeria and Atacama, by looking at the temporal evolution of the
744 ratios of the measured extinction coefficient in some specific mineral absorption bands. Changes
745 would indicate that the time variability of the mineralogical composition is optically significant. For
746 the Algeria case, we have considered the quartz (12.5 μm) versus clay (9.6 μm) bands, and for the
747 Atacama case the calcite (~7 μm) versus clay (9.6 μm) bands. For both cases, the calculated ratios do
748 not change significantly with time, i.e., they agree within error bars: for Algeria, the quartz-to-clay
749 ratio is 0.21±0.03 at the peak of the injection and 0.25±0.04 120 min later; for Atacama, the calcite-to-
750 clay ratio is 0.73±0.10 and 0.67±0.09 for the same times. Similar results were also obtained for the
751 other samples, with the exception of Saudi Arabia and Morocco, for which we observed an
752 increase of the calcite-to-clay ratio with time. The time invariance of the quartz-to-clays and calcite-to-
753 clays ratios observed for the majority of the analyzed aerosol samples agrees with the observations of
754 the size-dependent dust mineralogical composition obtained by Kandler et al. (2009). These authors
755 showed that in the super-micron diameter range up to ~25 μm, i.e., in the range where dust is mostly
756 LW-active, the quartz/clay and calcite/clay ratios are approximately constant with size. This would
757 suggest that the loss of particles in this size range should not modify the relative proportions of these

26

758 minerals, and thus their contributions to LW absorption. Nonetheless, the different behavior observed

759 for Saudi Arabia and Morocco would possibly indicate differences in the size-dependence of the min-

760 eralogical composition compared to the other samples.

761 For each soil, the estimated real (n) and imaginary (k) parts of the complex refractive index are shown

762 in Fig. 10. The reported n and k correspond to the mean of the 10-min values estimated between the

763 peak of the injection and 120 min later. This can be done because, for each soil, the time variation of

764 the complex refractive index is moderate. Standard deviations, ~~not shown in Fig. 10 for the sake of~~

765 ~~visual clarity,~~ are <10% for n and <20% for k. The d~~ata in Fig. 10 are reported by considering as error~~

766 ~~bar~~ the absolute uncertainty ~~on~~in n and k, previously estimated at ~20%. Figure 10 shows that the dust

767 refractive index widely varies both in magnitude and spectral shape from sample to sample, following

768 the variability of the measured extinction spectra. The values for the real part n ~~varies~~ span the

769 range~~between~~ 0.84 and 1.94, while the imaginary part k is between ~0.001 and 0.92. The imaginary

770 part, k, is observed to vary both from region to region, and also within ~~the same~~ each region. The dif-

771 ferences in k values obtained for different sources within the same region are ~~in fact~~ in most cases

772 larger than the estimated k uncertainties. For specific regions (Northern Africa, South America), the

773 variability for k is ~~approximately~~ of ~~the same~~a similar order of magnitude ~~of~~as the variability at the

774 global scale. Conversely, the n values mostly agree within error ~~bars~~ for all soils, both within ~~same~~a

775 region and from one region to another. Exceptions are observed only at wavelengths where strong sig-

776 natures from specific minerals are found in the n spectrum, as for example at 7 μm due to calcite ~~and~~

777 ~~seen for the~~ (Saudi Arabia and Gobi samples), or that of quartz at 9.2 μm (~~observed for~~ Patagonia and

778 Australia samples).

779

780

781 **6. Discussion**

782 **6.1 Predicting the dust refractive index based on its mineralogical composition**

783 Our results show that the LW refractive index of mineral dust having different mineralogical composi-

784 tions varies considerably. Nevertheless, at wavelengths where the absorption peaks due to different

785 minerals do not overlap, this variability can be predicted from the composition-resolved mass concen-

786 trations. These considerations are illustrated in Fig. 11a, where we relate the mean values of the dust k

787 in the calcite, quartz, and clay absorption bands between 7.0 and 11.4 μm to the percent mass fraction

788 of these minerals in the dust. Mean k values were calculated as averages over the filter sampling times.

789 For calcite and quartz (resonance peaks at 7.0, 9.2, and 11.4 μm), this relation is almost linear. These

790 two minerals are commonly large in grain size and well crystallized. Their quantification by XRD is

791 certain and they produce a strong and well-identified absorption peak in the LW. Nonetheless, there

792 seems to be a lower limit of the percent mass of calcite (around 5%) that gives rise to absorption at 7

793 μm, and therefore measurable k-values (Fig. 11). Conversely, at 11.4 μm, non-zero k-values are ob-

794 tained even in the absence of calcite, due to the interference of the calcite peak and the clay resonance

795 bands. At this wavelength the correlation between k and the calcite mass fraction is also very low.

796 Poorer or no correlation is found between k and the percent mass fraction in the absorption bands of

797 clays at 9.6 and 10.9 μm. This different behavior is not unexpected. Clay minerals such as kaolinite,

798 illite, smectite and chlorite are soil weathering products containing aluminiumaluminum and silicon in

799 a 1:1 or 1:2 ratio (tetrahedral or octahedral structure, respectively). As a consequence, the position of

800 their vibrational peaks is very similar (Dorschner et al., 1978; Querry, 1987, Glotch et al., 2007). In the

801 atmosphere, these minerals undergo aging by gas and water vapor adsorption (Usher et al., 2003;

802 Schuttlefield et al., 2007). As a result of the production conditions in the soils (weathering) and aging

803 in the atmosphere, their physical and chemical conditions (composition, crystallinity, aggregation

804 state) might differ from one soil to anthe other, and from that of mineralogical standards. That is the

805 reason why XRD measurements of clays in natural dust samples might be erroneous, and why we pre-

806 fer to estimate the clay fraction indirectly. Nonetheless, the indirect estimate is also prone to error, and

807 depends strongly on an independent estimate of the total mass (which, in the presence of large particles

808 can be problematic) as well as the correct quantification of the non-clay fraction. This is likely reflect-

809 ed in the large scatter observed in Fig. 11a when trying to relate the k-value distribution to the corre-

810 sponding percent mass of clays. These considerations also affect the speciation of clays, and explain

811 the similar results obtained when separately plotting the spectral k-values against the estimated kaolin-

812 ite or illite masses. The superposition of the resonance bands of these two clays, as well as those of the

813 smectites, which in addition are often poorly crystallized and therefore difficult to detect by XRD, as

814 well as those in the quartz absorption band at 9.2 μm, suggests that a more formal spectral deconvolu-

815 tion procedure based on single mineral reference spectra is needed to understand the shape and magni-

816 tude of the imaginary refractive index in this spectral band.

Similarly to Fig. 11a, ~~the~~ Fig. 11b shows the relationship between the mean values of the dust refractive index versus the percent mass fraction of calcite, quartz, and clays at 7.0, 9.2, 9.6, 10.9, and 11.4 µm for the real part. The correlation between n and the mineral percent mass fraction is found to be statistically significant only for the calcite band at 7.0 µm, while for all other cases, very poor or no correlation is found. The real refractive index of dust is also almost constant at all bands (with the exception of that at 7.0 µm) regardless of the change in particle composition.

6.2 Dust complex refractive index versus size distribution during atmospheric transport

Quantifying the radiative impact of dust depends not only on the ability to provide spatially-resolved optical properties, but also on the accurate representation of the possible changes of these properties during transport. In the LW, this effect is amplified by the changes in the size distribution, particularly the loss of coarse particles. Our experiments accurately capture the overall features of the dust size distribution, including the extent and modal position of the coarse particle mode. However, the depletion rate with time for coarse particles is higher than observed in the atmosphere (e.g., Ryder et al., 2013b). The size distribution after 30 minutes still contains a significant, relatively invariant, but not-predictable fraction of coarse particles. This calls for two considerations: 1) the refractive indices obtained at the early stage of the experiments (within 30 minutes after the dust injection) are representative of dust at short to medium ranges of transport (~1-2 days after emission); 2) the refractive indices after 30 minutes of duration are likely to represent long-range transported dust still containing coarse particles in a fraction that will depend on the original soil. In our study, the calculated refractive indices do not change with time in parallel with the observed changes in the size distribution, thus suggesting that a constant value can be assumed close to the source and ~~during~~ following transport. Still, further experiments taking into account only the fine fraction of the aerosols will be needed to constrain the size-dependence of the refractive index.

6.3 Comparison with the literature

In Fig. 12, we compare our results with estimates of the dust refractive index reported in the literature. We consider data by Volz (1972, 1973) for dust collected in Germany and at Barbados, Fouquart et al. (1987) for Niger sand, and Di Biagio et al. (2014a) for dust from Algeria and Niger. We also report

29

846   data for dust as assumed in the OPAC database (Optical Properties of Aerosols and Clouds; Hess et al.,

847   1998; Koepke et al., 2015). These literature data, in particular those of OPAC and Volz (1973), one

848   ofare the most frequently used references in climate modeling and remote sensing applications. Be-

849   cause of their limited regional span, the literature data clearly cannot do justice to the full range of

850   magnitude and of the spectral variability of the LW complex refractive index that is presented in our

851   dataset. In particular, clearly none of the published data represent the contribution of calcite at ~7 µm.

852   Some of the data (Volz, 1973; Fouquart et al., 1987; OPAC) overestimate k above 11 µm, where the

853   12.5-12.9 µm quartz absorption band is found. The best correspondence, especially above 10 µm, is

854   found with Di Biagio et al. (2014a). In the 8–12 µm atmospheric window, the agreement with our es-

855   timated mean value is moderate, but the range of variability around the mean and its spectral depend-

856   ence are underrepresented. A shift towards larger wavelengths is also observed for the main clay ab-

857   sorption peak at ~9.6 µm for Volz (1973) and Di Biagio et al. (2014a), which is possibly linked to the

858   different method used in these studies to retrieve the complex refractive index (pellet spectroscopy

859   approach) compared to our data. The agreement is even less satisfactory for the real part of the refrac-

860   tive index (upper panel of Fig. 12), which is overestimated in OPAC and Volz (1973) and underesti-

861   mated in Fouquart et al. (1987). As discussed in Di Biagio et al. (2014a), differences for the real part

862   between the various studies come mostly from the different methods used to estimate the dust refrac-

863   tive index. The methods used in the literature most often do not fulfil the Kramers-Kronig relationship

864   for the n-k couples. The only dataset that fulfils the Kramers-Kronig relationship is Fouquart et al.

865   (1987), but that has the drawback of underestimating n as a consequence of the low value of n_{vis} (~1)

866   assumed in the retrieval.

867   On average, the differences between our mean refractive index and the values reported in the literature

868   are large enough to have a significant effect on radiative transfer. For example, at 10 µm the absolute

869   difference between our retrieved mean k and the k by OPAC and Volz (1973) is between 0.15 and 0.6.

870   Highwood et al. (2003) have estimated that a change of about 0.3 in k at 10 µm, which corresponds to

871   half of the difference we have compared to Volz (1973), may determineresult in up to 3 K change in

872   the modelled sky brightness temperature, the quantity measured by infrared remote sensing. To give a

873   comparison term, the same order of brightness temperature difference at 10 µm was found between

874   clear sky and dusty conditions for an optical depth of ~1.5 at 0.55 µm. This example puts in evi-

875   denceillustrates the sensitivity of the brightness temperature to the differences in the imaginary part of

876   the refractive index that we find between our data and those in the literature. The brightness tempera-

30

877 ~~ture is the quantity measured by infrared remote sensing.~~ Another example, ~~indeed~~ of even more rele-
878 vance for climate applications, is provided by Di Biagio et al. (2014a), who have shown that a 0.3 var-
879 iation in k is sufficient to induce up to ~15% of change of the radiative forcing efficiency at 10 μm at
880 the TOA.

881

882 **7. Conclusions and perspectives**

883 In this study we have presented a new set of laboratory in-situ measurements of the LW extinction
884 spectra and complex refractive indices of mineral dust aerosols from nineteen natural soils from source
885 regions in Northern Africa, Sahel, Middle East, Eastern Asia, North and South America, Southern Af-
886 rica, and Australia. These sources are representative of the heterogeneity of the dust composition at the
887 global scale. Consequently, the envelope of refractive index data obtained in this study can adequately
888 represent the full range of variability for dust as function of the global variability of its mineralogical
889 composition. These data are expected to be widely applicable for both radiative transfer modelling and
890 remote sensing applications.

891 The experiments described here were conducted in the realistic and dynamic environment of the 4.2 m^3
892 CESAM chamber. Dust aerosols generated in the chamber are characterized by a realistic size distribu-
893 tion, including both the sub-micron and the super-micron fraction, and they have an atmospherically
894 representative mineralogical composition, including the main LW active minerals, such as quartz,
895 clays, and calcite. The complex refractive index of dust at LW wavelengths is obtained following a
896 rigorous approach that permits to determine n-k couples that satisfy the Kramers-Kronig relation. Re-
897 fractive index data from the present study are much more reliable than those provided by DB14, given
898 that a better estimate of n_{vis} was used in the retrieval algorithm. The average uncertainty in the ob-
899 tained n and k is ~20%.

900 The main results from this work can be summarized as follows.

901 1. The imaginary LW refractive index, k, of dust varies strongly both in magnitude and spectral shape
902   as a result of the variability of the particle mineralogy related to the specific ~~ource region of~~ emis-
903   sion sources. The value of k is observed to vary both from region to region, as well as within the
904   same region for varying sources. Conversely, for the real part n, values are observed to agree within
905   ~~the~~ error ~~bars~~ for the most part of the spectrum for all dust samples. This implies that while a con-

31

stant n can be taken for dust from different sources, a varying k should be used both at the global and at the regional scale. The available literature data (Volz, 1972, 1973; Fouquart et al., 1987; OPAC, Hess et al., 1998, Koepke et al., 2015) used nowadays in climate models and satellite retrievals, do not adequately represent either the magnitude, or the spectral features and the variability of the LW refractive index of mineral dust observed in our dataset. In consequence, we recommend the use of source-specific extinction spectra/imaginary refractive indices rather than generic values in models and remote sensing applications.

2. We observe a linear relationship between the magnitude of the imaginary LW refractive index and the mass concentration of specific minerals, i.e., quartz and calcite. This opens the possibility of providing predictive relationships to estimate the LW refractive index of dust at specific bands based on an assumed or predicted mineralogical composition, or conversely, to estimate the dust composition (even partially) from measurements of LW extinction at specific wavebands. This could have important implications for the representation of LW optical properties of dust in climate models, which have started to incorporate the representation of dust mineralogy in their schemes (Scanza et al., 2015; Perlwitz et al., 2015a). In addition, the possibility to relate the mass of minerals to the absorption at specific bands, such as for example the calcite band at ~7 μm, implies that the LW extinction spectra measured from space could be used to distinguish between different dust sources.

3. The spectral shape of the dust extinction spectrum does not seem to change significantly with time due toas a result of the loss of coarse particles by gravitational settling. This suggests that, despite the dust coarse mode being increasingly depleted, the relative proportions of minerals do not change significantly with time or at least that their changes do not affect the overall optical response of the dust samples. In consequence, the retrieved LW refractive index (real and imaginary) does not change, and therefore can be used to represent short-to-medium range transport conditions. This finding supports the common practice in global models to treat the dust LW refractive index as static during transport. This also implies that to represent the dust LW refractive index vs mineralogy, models just have to reproduce the dust composition at the source, without the necessity of following its changes during transport, which could be a challenge. This would considerably simplify the representation of dust mineralogy in models.

936 The unique dataset presented in this study should be particularly useful for improving the dust-climate
937 interactions within regional and global models, and to take into account the geographical variability of
938 the dust LW refractive index, which at present is not represented. This will allow obtaining a more
939 realistic representation of the dust LW effect and its radiative forcing upon climate. To date, as ~~evi-~~
940 ~~denced~~ shown in Boucher et al. (2013), even the sign of the dust direct effect remains unknown. In this
941 regard, ~~, in particular,~~ we estimate a lower dust absorption than ~~in~~ most of literature data (see k curves
942 in Fig. 12), and in particular than those of Volz (1973) and OPAC, ~~,~~ which are the reference data ~~mos-~~
943 ~~tre~~ frequently used in climate models ~~(see k curves in Fig. 12)~~. The integral of the Volz and OPAC
944 dust refractive ~~index~~ices (imaginary part) between 3 and 15 μm, for example, is about 15–20% larger
945 compared to the integral obtained from our max k curve; an up to about one order of magnitude over-
946 estimate is found when the integral of the Volz and OPAC k over the 3-15 μm range is compared to
947 the integral of our min k curve. ~~In~~ As a consequence of this, we can conclude that the use of the Volz
948 and OPAC data may introduce a systematic bias in modelling dust radiative effects at LW wave-
949 lengths.

950 The use of the data from the present study also will help to ~~reduce~~ing uncertainties in satellite retriev-
951 als, thus contributing to improv~~ing~~e the remote sensing capability over regions affected by dust (~~e.g.,~~
952 Clarisse et al., 2013; Vandenbussche et al., 2013; Capelle et al., 2014; Cuesta et al., 2015).

953 The work presented in this paper also opens various perspectives:~~.~~

954 First, as already pointed out, the results of the present study clearly suggest that the LW refractive in-
955 dex of dust varies at the regional scale, as can be observed in Fig. 10 for Northern Africa, Sahel, the
956 Middle East, Eastern Asia, South America and Southern Africa. For some particular regions, ~~as~~e.g.,
957 Northern Africa and South America, the extent of this variability is comparable to the variability ob-
958 tained at the global scale. The dust samples used in this study were chosen to cover the full heteroge-
959 neity of the dust composition at the global scale. However, the available samples do not necessarily
960 explore the possible full variability of the dust composition within each region. This regional variabil-
961 ity ~~This regional variability has to be characterized further~~ needs to be characterized further in order to
962 better assess the influence of dust on regional climate.

963 Second, the possibility of a more formal spectral deconvolution procedure based on single mineral
964 reference spectra to understand the shape, magnitude, and temporal variability of the refractive index

33

965 in all different spectral bands must be investigated. This could strongly help finding robust relation-
966 ships linking the dust refractive index to the particle mineralogy.

967 Third, further experimental efforts by increasing the lifetime and selecting size classes will be needed
968 to verify better the applicability of the obtained refractive ind~e~ices~x~ to long-range transport conditions.
969 Also, the experiments described here were done in conditions when dry deposition is the only aging
970 process. Other aging processes, such as heterogeneous reactions, mixing with other aerosol types, or
971 water uptake, have to be investigated to evaluate their impact on the LW refractive index during
972 transport. For instance, some studies suggest a possible enhancement of dust LW absorption over spe-
973 cific bands if water uptake occurs (Schuttlefield et al., 2007) or if dust mixes with soot (Hansell et al.,
974 2011).

975
976
977

978 **Appendix 1. Control experiment with ammonium sulfate particles**
979 In order to validate the methodology applied in this study, a control experiment was performed on
980 ammonium sulfate aerosols. Particles were generated from a 0.03 M solution of ammonium sulfate
981 using a constant output atomizer (TSI, model 3075). The aerosol flow passed through a diffusion drier
982 (TSI, model 3062), to be then injected in the CESAM chamber at a flow of 10 L min^{-1} for 10 minutes.
983 At the peak of the injection the aerosol concentration reached ~160 µg m^{-3} and the size distribution
984 was mono-modal and centered at ~0.06 µm. The LW spectrum of ammonium sulfate measured in
985 CESAM at the peak of the injection is shown in Fig. A1 for the 2-15 µm range. Absorption bands at-
986 tributed to gas-phase water vapor and CO_2 present in the chamber during the experiments are indicated
987 in the plot. The 2-15 µm spectral region includes three of the four active vibrational modes of ~the~ am-
988 monium sulfate ~salt~: $v_3(NH_4^+)$ (3230 cm^{-1} or 3.10 µm), $v_4(NH_4^+)$ (1425 cm^{-1} or 7.02 µm; not identified
989 in the plot due to its superposition with the water vapor band), and $v_3(SO_2^{-4})$ (1117 cm^{-1} or 8.95 µm).
990 The $v_4(SO_2^{-4})$ is at 620 cm^{-1} (16.12 µm), thus below the measurement range of the FTIR. The retrieval
991 algorithm described in Sect. 3 was applied to estimate the complex refractive index of ammonium sul-
992 fate aerosols. Calculations were performed only in the 8-10 µm range where the $v_3(SO_2^{-4})$ band is
993 found and where the contamination by water vapor is minimal. The value of n_{vis} to use as input to the
994 algorithm was set at 1.55, based on the analysis of simultaneous SW optical data (not discussed here).

34

995 The results of the calculations are shown in Fig. A1. The comparison with the optical constants pro-
996 vided by Toon et al. (1976), also shown in Fig. A1, is very satisfactory. A small bias is observed for
997 our retrieved n compared to the values by Toon et al. (1976). This can be possibly linked to the method
998 used in Toon et al. (1976) to retrieve the real part of the refractive index, which is based on the meas-
999 urement of the normal incident reflectivity of a bulk sample instead of absorption data of aerosol parti-
1000 cles, as in our experiments. Overall, the results of the control experiment indicate that the CESAM
1001 approach and the proposed retrieval algorithm allow ~~to~~ reprod~~uce~~ing the LW spectral signature of the
1002 aerosols and ~~to~~ estimat~~e~~ing accurately their complex refractive index.

1003

1004

1005

1006

1007

1008

1009

1010

1011

1012

1013

1014

1015 **Author contributions**

1016 C. Di Biagio, P. Formenti, Y. Balkanski, and J. F. Doussin designed the experiments and discussed the
1017 results. C. Di Biagio realized the experiments and performed the full data analysis with contributions
1018 by P. Formenti, L. Caponi, M. Cazaunau, E. Pangui, S. Caquineau, and J.F. Doussin. S. Nowak per-
1019 formed the XRD measurements. M. O. Andreae, K. Kandler, T. Saeed, S. Piketh, D. Seibert, and E.
1020 Williams collected the soil samples used for experiments. E. Journet participated to the selection of the

1021 soil samples for experiments and contributed to the scientific discussion. C. Di Biagio, P. Formenti,
1022 and Y. Balkanski wrote the manuscript with comments from all co-authors.

1023

1024 **Acknowledgements**

1039
1040
1041
1042
1043
1044
1045
1046
1047
1048
1049 **References**

36

Alfaro, S. C., Lafon, S., Rajot, J. L., Formenti, P., Gaudichet, A., and Maillé, M.: Iron oxides and light absorption by pure desert dust: an experimental study, J. Geophys. Res., 109, D08208, doi:10.1029/2003JD004374, 2004.

Balkanski, Y., Schulz, M., Claquin, T., and Guibert, S.: Reevaluation of mineral aerosol radiative forcings suggests a better agreement with satellite and AERONET data, Atmos. Chem. Phys., 7, 81–95, doi:10.5194/acp-7-81-2007, 2007.

Bohren, C. E. and Huffman, D. R.: Absorption and Scattering of Light by Small Particles, Wiley, New York, 1983.

Boucher, O., et al., Clouds and Aerosols. Stocker, T., & Qin, D. (eds), Climate Change 2013: The Physical Science Basis. Contribution of Working Group I to the Fifth Assessment Report of the Intergovernmental Panel on Climate Change. Cambridge Univ. Press, Cambridge, United Kingdom and New York, NY, USA, 2013.

Capelle, V., Chédin, A., Siméon, M., Tsamalis, C., Pierangelo, C., Pondrom, M., Crevoisier, C., Crepeau, L., and Scott, N. A.: Evaluation of IASI-derived dust aerosol characteristics over the tropical belt, Atmos. Chem. Phys., 14, 9343-9362, doi:10.5194/acp-14-9343-2014, 2014.

Caponi, L., Formenti, P., Massabó, D., Di Biagio, C., Cazaunau, M., Pangui, E., Chevailler, S., Landrot, G., Fonda, E., Andreae, M. O., B., Kandler, Piketh, S., Saeed, T., Seibert, D., Williams, E., Balkanski, Y., and Doussin, J.-F.: Spectral- and size-resolved mass absorption cross-sections of mineral dust aerosols in the shortwave: a smog chamber study, Atmos. Chem. Phys. Discuss., submitted.

Caquineau, S., Magonthier, M. C., Gaudichet, A., and Gomes, L.: An improved procedure for the X-ray diffraction analysis of low-mass atmospheric dust samples, Eur. J. Mineral., 9, 157–166, 1997.

Caquineau, S., Gaudichet, A., Gomes, L., and Legrand, M.: Mineralogy of Saharan dust transported over northwestern tropical Atlantic Ocean in relation to source regions, J. Geophys. Res., 107(D15), 4251, doi:10.1029/2000JD000247, 2002.

Claquin, T., Schulz, M., Balkanski, Y. J., and Boucher, O.: Uncertainties in assessing radiative forcing by mineral dust, TellusB, 50, 491–505, 1998.

Claquin, T., Schulz, M., and Balkanski, Y. J.: Modeling the mineralogy of atmospheric dust sources, J. Geophys. Res., 104, 22243-22256, 1999.

Clarke, A. D., Shinozuka, Y. V., Kapustin, N., Howell, S., Huebert, B., Doherty, S.,Anderson, T., Covert, D., Anderson, J., Hua, X., Moore II, K. G., McNaughton, C., Carmichael, G., and Weber, R.: Size distributions and mixtures of dust and black carbon aerosol in Asian outflow: Physiochemistry and optical properties, J. Geophys. Res., 109, D15S09, doi:10.1029/2003JD004378, 2004.

Clarisse, L., Coheur, P.-F., Prata, F., Hadji-Lazaro, J., Hurtmans, D., and Clerbaux, C.: A unified approach to infrared aerosol remote sensing and type specification, Atmos. Chem. Phys., 13, 2195-2221, doi:10.5194/acp-13-2195-2013, 2013.

37

1088 Colarco, P. R., Nowottnick, E. P., Randles, C. A., Yi, B., Yang, P., Kim, K.-M., Smith, J. A., and Bar-
1089   deen, C. G.: Impact of radiatively interactive dust aerosols in the NASA GEOS-5 climate model:
1090   Sensitivity to dust particle shape and refractive index, J. Geophys. Res. Atmos., 119, 753–786,
1091   doi:10.1002/2013JD020046, 2014.

1092 Cuesta, J., Eremenko, M., Flamant, C., Dufour, G., Laurent, B., Bergametti, G., Hopfner, M., Orphal,
1093   J., and Zhou, D.: Three-dimensional distribution of a major desert dust outbreak over East Asia in
1094   March 2008 derived from IASI satellite observations, J. Geophys. Res., 120, 7099-7127, 2015.

1095 Davies, C. N. : Particle-fluid interaction, J. Aerosol. Sci., 10, 477–513, 1979.

1096 Denjean, C., Cassola, F., Mazzino, A., Triquet, S., Chevaillier, S., Grand, N., Bourrianne, T., Mom-
1097   boisse, G., Sellegri, K., Schwarzenbock, A., Freney, E., Mallet, M., and Formenti, P.: Size distribu-
1098   tion and optical properties of mineral dust aerosols transported in the western Mediterranean, At-
1099   mos. Chem. Phys., 16, 1081-1104, doi:10.5194/acp-16-1081-2016, 2016.

1100 DeSouza-Machado, S. G., Strow, L. L., Hannon, S. E., and Motteler, H. E.: Infrared dust spectral sig-
1101   natures from AIRS, Geophy. Res. Lett., 33(L03801), 1-5, 2006.

1102 Di Biagio, C., Boucher, H., Caquineau, S., Chevaillier, S., Cuesta, J., and Formenti, P.: Variability of
1103   the infrared complex refractive index of African mineral dust: experimental estimation and implica-
1104   tions for radiative transfer and satellite remote sensing, Atmos. Chem. Phys., 14, 11093–11116,
1105   2014a.

1106 Di Biagio, C., P. Formenti, S. A. Styler, E. Pangui, and J.-F. Doussin: Laboratory chamber measure-
1107   ments of the longwave extinction spectra and complex refractive indices of African and Asian min-
1108   eral dusts, Geophys. Res. Lett., 41, 6289-6297, doi:10.1002/2014GL060213, 2014b.

1109 Di Biagio, C., P. Formenti, Y. Balkanski, L. Caponi, M. Cazaunau, E. Pangui, J.-F. Doussin, et al.:
1110   Global scale variability of the mineral dust shortwave refractive index and relationship to iron
1111   content, in preparation.

1112 di Sarra, A., Di Biagio, C., Meloni, D., Monteleone, F., Pace, G., Pugnaghi, S., and Sferlazzo, D.:
1113   Shortwave and longwave radiative effects of the intense Saharan dust event of March 25-26, 2010,
1114   at Lampedusa (Mediterranean sea), J. Geophys. Res., 116, D23209, doi:10.1029/2011JD016238,
1115   2011.

1116 Dorschner, J., Friedemann, C., and Guertler, J.: Laboratory spectra of phyllosilicates and the interstel-
1117   lar 10-micrometer absorption band, Astron. Nachr., 299, 269 – 282, 1978.

1118 Dubovik, O., Sinyuk, A., Lapyonok, T., Holben, B.N., Mishchenko, M., Yang, P., Eck, T.F., Volten,
1119   H., Muñoz, O., Veihelmann, B., van der Zande, W.J., Leon, J. F., Sorokin, M., and Slutsker, I.: Ap-
1120   plication of spheroid models to account for aerosol particle nonsphericity in remote sensing of de-
1121   sert dust. J. Geophys. Res., 111, D11208, doi:10.1029/2005JD006619, 2006.

1122 Dufresne, J.-L., Gautier, C., Ricchiazzi, P., and Fouquart, Y.: Longwave scattering effects of mineral
1123   aerosols, J. Atmos. Sci., 59, 1959–1966, 2002.

1124 Flores, J. M., Trainic, M., Borrmann, S., and Rudich, Y.: Effective broadband refractive index retrieval
1125   by a white light optical particle counter, Phys. Chem. Chem. Phys., 11, 7943–7950, 2009.

1126 Formenti, P., Rajot, J. L., Desboeufs, K., Said, F., Grand, N., Chevaillier, S., and Schmechtig, C.: Air-

1127   borne observations of mineral dust over western Africa in the summer Monsoon season: spatial and
1128   vertical variability of physico-chemical and optical properties, Atmos. Chem. Phys., 11, 6387-6410,
1129   doi:10.5194/acp-11-6387-2011, 2011.

1130   Formenti, P., Caquineau, S., Desboeufs, K., Klaver, A., Chevaillier, S., Journet, E., and Rajot, J. L.:
1131   Mapping the physico-chemical properties of mineral dust in western Africa: mineralogical composi-
1132   tion, Atmos. Chem. Phys., 14, 10663-10686, doi:10.5194/acp-14-10663-2014, 2014.

1133   Fouquart, Y., Bonnel, B., Brogniez, G., Buriez, J. C., Smith, L., and Morcrette, J. J.: Observations of
1134   Sahara aerosols: Results of ECLATS field experiment. Part II: Broadband radiative characteristics
1135   of the aerosols and vertical radiative flux divergence, J. Climate Appl. Meteor., 26, 38-52, 1987.

1136   Ginoux, P., Prospero, J. M., Gill, T. E., Hsu, N. C., and Zhao, M.: Global-scale attribution of anthro-
1137   pogenic and natural dust sources and their emission rates based on MODIS Deep Blue aerosol
1138   products, Rev. Geophys., 50, RG3005, doi:10.1029/2012RG000388, 2012.

1139   Glotch, T. D., Rossman, G. R., and Aharonson, O.: Mid-infrared (5–100 μm) reflectance spectra and
1140   optical constants of ten phyllosilicate minerals, Icarus, 192, 604–622, 2007.

1141   Goudie, A. S., and Middleton, N. J.: Saharan dust storms: Nature and consequences, Earth-Sci. Rev.,
1142   56, 179–204, 2001.

1143   Goudie A. S., and Middleton, N. J.: Desert dust in the global system. Springer, Berlin, Heidelberg,
1144   New York, 2006.

1145   Hansell, Jr., R. A., Reid, J. S., Tsay, S. C., Roush, T. L., and Kalashnikova, O. V.: A sensitivity study
1146   on the effects of particle chemistry, asphericity and size on the mass extinction efficiency of min-
1147   eral dust in the earth's atmosphere: from the near to thermal IR, Atmos. Chem. Phys., 11, 1527-
1148   1547, doi:10.5194/acp-11-1527-2011, 2011.

1149   Hess, M., Koepke, P., and Schult, I.: Optical properties of aerosols and clouds: The software package
1150   OPAC, Bull. Am. Meteorol. Soc, 79, 831–844, 1998.

1151   Highwood, E. J., Haywood, J. M., Silverstone, M. D., Newman, S. M., and Taylor, J. P.: Radiative
1152   properties and direct effect of Saharan dust measured by the C-130 aircraft during Saharan Dust
1153   Experiment (SHADE): 2. Terrestrial spectrum, J. Geophys. Res., 108, 8578,
1154   doi:10.1029/2002JD002552, 2003.

1155   Hsu, N. C., Herman, J. R., and Weaver, C. J.: Determination of radiative forcing of Saharan dust using
1156   combined TOMS and ERBE data, J. Geophys. Res., 105(D16), 20,649–20,661,
1157   doi:10.1029/2000JD900150, 2000.

1158   Israelevich, P. L., Levin, Z., Joseph, J. H., and Ganor, E.: Desert aerosol transport in the Mediterranean
1159   region as inferred from the TOMS aerosol index, J. Geophys. Res., 107 (D21), 4572,
1160   doi:10.1029/2001JD002011, 2002.

1161   Jeong, G. Y., Bulk and single-particle mineralogy of Asian dust and a comparison with its source soils,
1162   J. Geophys. Res., 113, D02208, doi:10.1029/2007JD008606, 2008.

1163   Journet, E., Balkanski, Y., and Harrison, S. P.: A new data set of soil mineralogy for dust-cycle model-
1164   ing, Atmos. Chem. Phys., 14, 3801-3816, doi:10.5194/acp-14-3801-2014, 2014.

Mis en forme : Espace Après : 0.2 pt

Kaaden, N., Massling, A., Schladitz, A., Müller, T., Kandler, K., Schütz, L., Weinzierl, B., Petzold, A., Tesche, M., Leinert, S., and Wiedensohler, A.: State of Mixing, Shape Factor, Number Size Distribution, and Hygroscopic Growth of the Saharan Anthropogenic and Mineral Dust Aerosol at Tinfou, Morocco, Tellus B, 61, 51–63, 2009.

Kalashnikova, O. V. and Sokolik, I. N.: Modeling the radiative properties of nonspherical soil-derived mineral aerosols, J. Quant. Spectrosc. Radiat. Transfer, 87, 137–166, 2004.

Karyampudi, V. M., Palm, S. P., Reagen, J. A., Fang, H., Grant, W. B., Moff, H. R., Moulin, C., Pierce, H. F., Torres, O., Browell, E. V., and Melfi, S. H.: Validation of the Saharan dust plume conceptual model using lidar, Meteosat, and ECMWF data., Bull. Am. Meteorol. Soc., 80, 1045–1075, 1999.

Kandler, K., Schütz, L., Deutscher, C., Ebert, M., Hofmann, H., Jäckel, S., Jaenicke, R., Knippertz, P., Lieke, K., Massling, A., Petzold, A., Schladitz, A.,Weinzierl, B.,Wiedensohler, A., Zorn, S., and Weinbruch, S.: Size distribution, mass concentration, chemical and mineralogical composition and derived optical parameters of the boundary layer aerosol at Tinfou, Morocco, during SAMUM 2006, Tellus B, 61, 32–50, doi:10.1111/j.1600-0889.2008.00385.x, 2009.

Kim, D., Chin, M., Yu, H., Eck, T. F., Sinyuk, A., Smirnov, A., and Holben, B.: Dust optical properties over North Africa and Arabian Peninsula derived from the AERONET dataset, Atmos. Chem. Phys., 11, 10733–10741, doi:10.5194/acp-11-10733-2011, 2011.

Klaver, A., Formenti, P., Caquineau, S., Chevaillier, S., Ausset, P., Calzolai, G., Osborne, S., Johnson, B., Harrison, M., and Dubovik, O.: Physico-chemical and optical properties of Sahelian and Saharan mineral dust: in situ measurements during the GERBILS campaign, Q. J. Roy. Meteor. Soc., 137, 1193–1210, doi:10.1002/qj.889, 2011.

Klüser, L., Martynenko, D., and Holzer-Popp, T.: Thermal infrared remote sensing of mineral dust over land and ocean: a spectral SVD based retrieval approach for IASI, Atmos. Meas. Tech., 4, 757–773, 2011.

Koepke, P., Gasteiger, J., and Hess, M.: Technical Note: Optical properties of desert aerosol with non-spherical mineral particles: data incorporated to OPAC, Atmos. Chem. Phys., 15, 5947-5956, doi:10.5194/acp-15-5947-2015, 2015.

Lafon, S., Sokolik, I. N., Rajot, J. L., Caquineau, S., and Gaudichet, A.: Characterization of iron oxides in mineral dust aerosols: Implications for light absorption, J. Geophys. Res., 111, D21207, 10.1029/2005jd007016, 2006.

Laskina, O., Young, M. A., Kleiber, P. D., and Grassian, V. H.: Infrared extinction spectra of mineral dust aerosol: single components and complex mixtures, J. Geophys. Res., 117, D18210, doi:10.1029/2012JD017756, 2012.

Legrand, M., Dubovik, O., Lapyonok, T., and Derimian, Y.: Accounting for particle non-sphericity in modeling of mineral dust radiative properties in the thermal infrared, J. Quant. Spectros. Rad. Transf., 149, 219–240, 2014.

Leon, J-F., and Legrand, M.: Mineral dust sources in the surroundings of the north Indian Ocean, Geophys. Res. Lett., doi: 10.1029/2002GL016690, 2003.

Lepple, F. K. and Brine, C. J.: Organic constituents in eolian dust and surface sediments from northwest Africa, J. Geophys. Res., 81, 1141–1147, 1976.

Liao, H. and Seinfeld, J. H.: Radiative forcing by mineral dust aerosols: sensitivity to key variables, J. Geophys. Res., 103(D24), 31 637–31 646, doi:10.1029/1998JD200036, 1998.

Long, L. L., Querry, M. R., Bell, R. J., and Alexander, R. W.: Optical properties of calcite and gypsum in crystalline and powdered form in the infrared and far-infrared, Infrared Physics, 34, 191-201, 1993.

Maddy, E. S., DeSouza-Machado, S. G., Nalli, N. R., Barnet, C. D., Strow, L. L., Wolf, W. W., Xie, H., Gambacorta, A., King, T. S., Joseph, E., Morris, V., Hannon, S. E., and Schou, P.: On the effect of dust aerosols on AIRS and IASI operational level 2 products, Geophys. Res. Lett., 39, L10809, doi:10.1029/2012GL052070, 2012.

Marticorena, B., Chatenet, B., Rajot, J. L., Traoré, S., Coulibaly, M., Diallo, A., Koné, I., Maman, A., Ndiaye, T., and Zakou, A.: Temporal variability of mineral dust concentrations over West Africa: analyses of a pluriannual monitoring from the AMMA Sahelian Dust Transect, Atmos. Chem. Phys., 10, 8899–8915, 2010.

Maring, H., Savoie, D. L., Izaguirre, M. A., Custals, L., and Reid, J. S.: Mineral dust aerosol size distribution change during atmospheric transport, J. Geophys. Res., 108, 8592, doi:10.1029/2002jd002536, 2003.

McConnell, C. L., Formenti, P., Highwood, E. J., and Harrison, M. A. J.: Using aircraft measurements to determine the refractive index of Saharan dust during the DODO Experiments, Atmos. Chem. Phys., 10, 3081–3098, doi:10.5194/acp-10-3081-2010, 2010.

McMurry, P. H., and Rader, D. J.: Aerosol Wall Losses in Electrically Charged Chambers, Aerosol Sci. Tech., 4:3, 249-268, 1985.

Meloni, D., Junkermann, W., di Sarra, A., Cacciani, M., De Silvestri, L., Di Iorio, T., Estellés, V., Gómez-Amo, J. L., Pace, G., and Sferlazzo, D. M.: Altitude-resolved shortwave and longwave radiative effects of desert dust in the Mediterranean during the GAMARF campaign: Indications of a

net daily cooling in the dust layer. J. Geophys. Res. Atmos., 120, 3386–3407. doi: 10.1002/2014JD022312, 2015.

Miller, R. L., Knippertz, P., Pérez García-Pando, C., Perlwitz, J. P., and Tegen, I.: Impact of dust radiative forcing upon climate. In Mineral Dust: A Key Player in the Earth System. P. Knippertz, and J.-B.W. Stuut, Eds. Springer, 327-357, doi:10.1007/978-94-017-8978-3_13, 2014.

Osada, K., Ura, S., Kagawa, M., Mikami, M., Tanaka, T. Y., Matoba, S., Aoki, K., Shinoda, M., Kurosaki, Y., Hayashi, M., Shimizu, A., and Uematsu, M.: Wet and dry deposition of mineral dust particles in Japan: factors related to temporal variation and spatial distribution, Atmos. Chem. Phys., 14, 1107–1121, doi: 10.5194/acp-14-1107-2014, 2014.

Osborne, S. R., Johnson, B. T., Haywood, J. M., Baran, A. J., Harrison, M. A. J., and McConnell, C. L.: Physical and optical properties of mineral dust aerosol during the Dust and Biomass-burning Experiment, J. Geophys. Res., 113, D00C03, doi:10.1029/2007jd009551, 2008.

Otto, S., Bierwirth, E., Weinzierl, B., Kandler, K., Esselborn, M., Tesche, M., Schladitz, A.,Wendisch, M., and Trautmann, T.: Solar radiative effects of a Saharan dust plume observed during SAMUM assuming spheroidal model particles, Tellus B, 61, 270–296, doi:10.1111/j.1600-0889.2008.00389.x, 2009.

Perlwitz, J. P., Pérez García-Pando, C., and Miller, R. L.: Predicting the mineral composition of dust aerosols — Part 1: Representing key processes. Atmos. Chem. Phys., 15, 11593-11627, doi:10.5194/acp-15-11593-2015, 2015a.

Perlwitz, J. P., Pérez García-Pando, C., and Miller, R. L.: Predicting the mineral composition of dust aerosols – Part 1: Model evaluation and identification of key processes with observations Representing key processes, Atmos. Chem. Phys. Discuss., 15, 3493-3575, doi:10.5194/acpd-15-3493-2015, 2015b.

Peterson, J. T., and Weinman, J. A.: Optical properties of quartz dust particles at infrared wavelengths, Geophys. Res. Lett., 74, 6947-6952, 1969.

Prospero, J. M., Ginoux, P., Torres, O., Nicholson, S. E., and Gill, T. E.: Environmental characterization of global sources of atmospheric soil dust identified with the Nimbus 7 Total Ozone Mapping Spectrometer (TOMS) absorbing aerosol product, Rev Geophys, 40, 1002, 2002.

Pye, K.: Aeolian Dust and Dust Deposits, Academic Press, London, 334 pp., 1987.

Querry, M.: Optical Constants of Minerals and Other Materials from the Millimeter to the Ultraviolet, Report CRDEC-CR-88009, US Army, Aberdeen, 1987.

Rajot, J. L., Formenti, P., Alfaro, S., Desboeufs, K., Chevaillier, S., Chatenet, B., Gaudichet, A., Journet, E., Marticorena, B., Triquet, S., Maman, A., Mouget, N., and Zakou, A.: AMMA dust exper-

42

1284   iment: an overview of measurements performed during the dry season special observation period
1285   (SOP0) at the Banizoumbou (Niger) supersite, J. Geophys. Res., 113, D00C14,
1286   doi:10.1029/2008jd009906, 2008.

1287 Reid, E. A., Reid, J. S., Meier, M. M., Dunlap, M. R., Cliff, S. S., Broumas, A., Perry, K., and Maring,
1288   H.: Characterization of African dust transported to Puerto Rico by individual particle and size seg-
1289   regated bulk analysis, J. Geophys. Res., 108, 8591, doi:10.1029/2002jd002935, 2003.

1290 Reid, J. S., Reid, E. A., Walker, A., Piketh, S., Cliff, S., Mandoos, A. A., Tsay, S.-C., and Eck, T. F.:
1291   Dynamics of southwest Asian dust particle size characteristics with implications for global dust re-
1292   search, J. Geophys. Res., 113, doi:10.1029/2007JD009752, 2008.

1293 Ryder, C. L., Highwood, E. J., Rosenberg, P. D., Trembath, J., Brooke, J. K., Bart, M., Dean, A., Cro-
1294   sier, J., Dorsey, J., Brindley, H., Banks, J., Marsham, J. H., McQuaid, J. B., Sodemann, H., and
1295   Washington, R.: Optical properties of Saharan dust aerosol and contribution from the coarse mode
1296   as measured during the Fennec 2011 aircraft campaign, Atmos. Chem. Phys., 13, 303–325, 2013a.

1297 Ryder, C. L., Highwood, E. J., Lai, T. M., Sodemann, H., and Marsham, J. H: Impact of atmospheric
1298   transport on the evolution of microphysical and optical properties of Saharan dust, Geophys. Res.
1299   Lett., 40, 2433–2438, doi:10.1002/grl.50482, 2013b.

1300 Scanza, R. A., Mahowald, N., Ghan, S., Zender, C. S., Kok, J. F., Liu, X., Zhang, Y., and Albani, S.:
1301   Modeling dust as component minerals in the Community Atmosphere Model: development of
1302   framework and impact on radiative forcing, Atmos. Chem. Phys., 15, 537-561, doi:10.5194/acp-15-
1303   537-2015, 2015.

1304 Scheuvens, D., L. Schütz, K. Kandler, M. Ebert, and S. Weinbruch, Bulk composition of northern Af-
1305   rican dust and its source sediments - A compilation, Earth-Sci. Rev., 116, 170-194, 2013.

1306 Schuttlefield, J. D., Cox, D. and Grassian, V. H.: An investigation of water uptake on clays minerals
1307   using ATR-FTIR spectroscopy coupled with quartz crystal microbalance measurements, J. Ge-
1308   ophys. Res., 112, D21303, doi:10.1029/2007JD00897, 2007.

1309 Schütz, L., and Jaenicke, R.: Particle Number and Mass Distributions above 10^{-4} cm Radius in Sand
1310   and Aerosol of the Sahara Desert, J. Appl. Meteorol., 13, 863-870, 10.1175/1520-
1311   0450(1974)013<0863:PNAMDA>2.0.CO;2, 1974.

1312 Schütz, L., Jaenicke, R., and Pietrek, H.: Saharan dust transport over the North Atlantic Ocean, Geol.
1313   Soc. Am. Spec. Paper, 186, 87-100, 10.1130/SPE186-p87, 1981.

1314 Seinfeld, J. H., and Pandis, S. N.: Atmospheric Chemistry and Physics: From Air Pollution to Climate
1315   Change, Wiley, New York, 2006.

1316 Sertsu, S. M., and Sánchez, P. A.: Effects of Heating on Some Changes in Soil Properties in Relation
1317   to an Ethiopian Land Management Practice, Soil Sci. Soc. Am. J., 42, 940-944, 1978.

1318 Shen, Z. X., Li, X., Cao, J., Caquineau, S., Wang, Y., and Zhang, X.: Characteristics of clay minerals
1319   in Asian dust and their environmental significance, China Particuology, 3, 260–264, 2005.

1320 Slingo, A., Ackerman, T. P., Allan, R. P., Kassianov, E. I., McFarlane, S. A., Robinson, G. J., Barnard,
1321   J. C., Miller, M. A., Harries, J. E., Russell, J. E., and Dewitte, S.: Observations of the impact of a

1322 major Saharan dust storm on the atmospheric radiation balance, Geophys. Res. Lett., 33, L24817,
1323 doi:10.1029/2006GL027869, 2006.

1324 Sokolik I. N., Andronova, A. V., and Jonhson, T. C.: Complex refractive index of atmospheric dust
1325 aerosols, Atmos. Environ., 16, 2495–2502, 1993.

1326 Sokolik, I. N. and Toon, O. B.: Direct radiative forcing by anthropogenic airborne mineral aerosols,
1327 Nature, 381, 681–683, 1996.

1328 Sokolik, I. N., Toon, O. B., Bergstrom, R. W.: Modeling the radiative characteristics of airborne min-
1329 eral aerosols at infrared wavelengths, J. Geophy. Res., 103 : 8813-8826, 1998.

1330 Sokolik, I., and Toon, O.: Incorporation of mineralogical composition into models of the radiative
1331 properties of mineral aerosol from UV to IR wavelengths, J. Geophys. Res., 104(D8), 9423-9444,
1332 1999.

1333 Sokolik, I. N.: The spectral radiative signature of windblown mineral dust: implications for remote
1334 sensing in the thermal IR region, Geophys. Res. Lett., 29, 2154, doi:10.1029/2002GL015910, 2002.

1335 Tegen, I. and Lacis, A. A.: Modeling of particle size distribution and its influence on the radiative
1336 properties of mineral dust aerosol,, J. Geophys. Res., doi: 10.1029/95JD03610, 1996.

1337 Toon, O. B., Pollack, J. B., and Khare, B. N.: The Optical Constants of Several Atmospheric Aerosol
1338 Species: Ammonium Sulfate, Aluminum Oxide, and Sodium Chloride, J. Geophys. Res., 81, 5733–
1339 5748, 1976.

1340 Usher, C. R., Michel , A. E., and Grassian, V. H.: Reactions on mineral dust, Chem. Rev., 103, 4883–
1341 4939, 2003.

1342 Vandenbussche, S., Kochenova, S., Vandaele, A. C., Kumps, N., and De Mazière, M.: Retrieval of
1343 desert dust aerosol vertical profiles from IASI measurements in the TIR atmospheric window, At-
1344 mos. Meas. Tech., 6, 2577-2591, doi:10.5194/amt-6-2577-2013, 2013.

1345 Vickery, K. J., Eckardt, F. D. and Bryant, R. G.: A sub-basin scale dust plume source frequency inven-
1346 tory for southern Africa, 2005–2008, Geophys. Res. Lett., 40, 5274–5279, doi:10.1002/grl.50968,
1347 2013.

1348 Volz, F. E.: Longwave refractive index of atmospheric aerosol substances, Appl. Optics, 11, 755-759,
1349 1972.

1350 Volz, F. E.: Longwave optical constants of ammonium sulfate, Sahara dust; volcanic pumice and
1351 flyash, Appl. Optics., 12, 564-568, 1973.

1352 von der Weiden, S.-L., Drewnick, F., and Borrmann, S.: Particle Loss Calculator – a new software tool
1353 for the assessment of the performance of aerosol inlet systems, Atmos. Meas. Tech., 2, 479–494,
1354 2009.

1355 Wang, J., Doussin, J. F., Perrier, S., Perraudin, E., Katrib, Y., Pangui, E., and Picquet-Varrault, B.:
1356 Design of a new multi-phase experimental simulation chamber for atmospheric photosmog, aerosol
1357 and cloud chemistry research, Atmos. Meas. Tech., 4, 2465–2494, 2011.

44

1358 Washington, R., Todd, M. C., Middleton, N., Goudie, A. S.: Dust-storm source areas determined by
1359   the Total Ozone Monitoring Spectrometer and surface observations, Ann. Assoc. Am. Geogr., 93,
1360   297–313, 2003.

1361 Weinzierl, B., Petzold, A., Esselborn, M., Wirth, M., Rasp, K., Kandler, K., Schutz, L., Koepke, P.,
1362   and Fiebig, M.: Airborne measurements of dust layer properties, particle size distribution and mix-
1363   ing state of Saharan dust during SAMUM 2006, Tellus, 61B, 96-117, doi:10.1111/j.1600-
1364   0889.2008.00392.x, 2009.

1365 White, J. U.: Long optical path of large aperture, J. Opt. Soc. Am., 32, 285–288, 1942.

1366

1367 Yang, E.-S., Gupta, P. and Christopher S. A.: Net radiative effect of dust aerosols from satellite meas-
1368   urements over Sahara, Geophys. Res. Lett., 36, L18812, doi:10.1029/2009GL039801, 2009.

1369

1370
1371
1372
1373
1374
1375
1376
1377
1378
1379
1380
1381
1382
1383
1384
1385
1386
1387
1388
1389
1390
1391
1392
1393
1394
1395
1396
1397
1398
1399
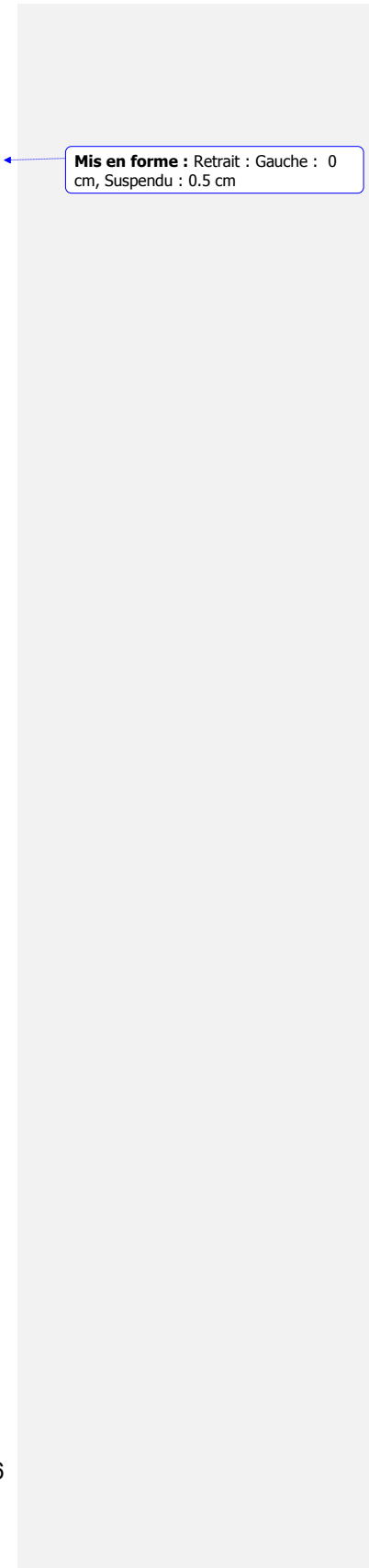
Mis en forme : Retrait : Gauche : 0 cm, Suspendu : 0.5 cm

Tables

Table 1. Measured and retrieved quantities and their estimated uncertainties. For further details refer to Sect. 2.

Parameter		Uncertainty	Uncertainty calculation
Optical LW	Transmission 2-16 μm, T	<10%	Quadratic combination of noise (~1%) and standard deviation over 10-min (5-10%)

Category	Parameter	Uncertainty	Method
	Extinction coefficient 2-16 μm, $\beta_{ext}(\lambda) = \dfrac{-\ln(T(\lambda))}{x}$	~10%	Error propagation formula[1] considering uncertainties on the measured transmission T and the optical path x (~2%)
Size distribution	SMPS geometrical diameter (D_g), $D_g = D_m / \chi$	~6%	Error propagation formula[1] considering the uncertainty on the estimated shape factor χ (~6%)
	SkyGrimm geometrical diameter (D_g)	<15.2%	Standard deviation of the D_g values obtained for different refractive indices values used in the optical to geometrical conversion
	WELAS geometrical diameter (D_g)	~5-7%	The same as for the SkyGrimm
	$\left[dN/d\log D_g\right]_{Corr,WELAS} = \left[dN/d\log D_g\right]/\left[1 - L_{WELAS}(D_g)\right]$	~20-70%	Error propagation formula[1] considering the $dN/d\log D_g$ st. dev. over 10-min and the uncertainty on L_{WELAS} (~50% at 2 μm, ~10% at 8 μm)
	$\left[dN/d\log D_g\right]_{filter} = \left[dN/d\log D_g\right]_{CESAM} * \left[1 - L_{filter}(D_g)\right]$	~25-70%	Error propagation formula[1] considering the uncertainties on $(dN/d\log D_g)_{CESAM}$ and L_{filter} (~55% at 2 μm, ~10% at 12 μm)
Mineralogical composition	Clays mass ($m_{Clay} = M_{total} - m_Q - m_F - m_C - m_D - m_G$)	8-26%	Error propagation formula[1] considering the uncertainty on M_{total} (4-18%) and that on m_Q, m_F, m_C, m_D, and m_G
	Quartz mass ($m_Q = S_Q / K_Q$)	9%	Error propagation formula[1] considering the uncertainty on the DRX surface area S_Q (~2%) and K_Q (9.4%)
	Feldspars mass ($m_F = S_F / K_F$)	14% (orthose), 8% (albite)	The same as for the quartz, K_F uncertainty 13.6% (orthose) and 8.4% (albite)
	Calcite mass ($m_C = S_C / K_C$)	11%	The same as for the quartz, K_C uncertainty 10.6%
	Dolomite mass ($m_D = S_D / K_D$)	10%	The same as for the quartz, K_D uncertainty 9.4%
	Gypsum mass ($m_G = S_G / K_G$)	18%	The same as for the quartz, K_G uncertainty 17.9%

1404   [1] $\sigma_f = \sqrt{\sum_{i=1}^{n}\left(\dfrac{\partial f}{\partial x_i}\sigma_{x_i}\right)^2}$

1405   **Table 2.** Summary of information on the soil samples used in this study.

1406
1407

Sample name	Collection Coordinates	Geographical zone	Country	Desert zone
Tunisia	33.02°N, 10.67°E	Northern Africa	Tunisia	Saharan desert (Maouna)
Morocco	31.97°N, 3.28°W	Northern Africa	Morocco	Saharan desert (east of Ksar Sahli)

Libya	27.01°N, 14.50°E	Northern Africa	Libya	Sahara desert (Sebha)
Algeria	23.95°N, 5.47°E	Northern Africa	Algeria	Saharan desert (Ti-n-Tekraouit)
Mauritania	20.16°N, 12.33°W	Northern Africa	Mauritania	Saharan desert (east of Aouinet Nchir)
Niger	13.52°N, 2.63°E	Sahel	Niger	Sahel (Banizoumbou)
Mali	17.62°N, 4.29°W	Sahel	Mali	Sahel (Dar el Beida)
Bodélé	17.23°N, 19.03°E	Sahel	Chad	Bodélé depression
Ethiopia	7.50°N, 38.65°E	Eastern Africa and the Middle East	Ethiopia	Lake Shala National Park
Saudi Arabia	27.49°N, 41.98°E	Eastern Africa and the Middle East	SaudiArabia	Nefud desert
Kuwait	29.42°N, 47.69°E	Eastern Africa and the Middle East	Kuwait	Kuwaiti desert
Gobi	39.43°N, 105.67°E	Eastern Asia	China	Gobi desert
Taklimakan	41.83°N, 85.88°E	Eastern Asia	China	Taklimakan desert
Arizona	33.15 °N, 112.08°W	North America	Arizona	Sonoran desert
Atacama	23.72°S, 70.40°W	South America	Chile	Atacama desert
Patagonia	50.26°S, 71.50°W	South America	Argentina	Patagonian desert
Namib-1	21.24°S, 14.99°E	Southern Africa	Namibia	Namib desert (area between the Kuiseb and Ugab valleys)
Namib-2	19.0°S, 13.0°E	Southern Africa	Namibia	Namib desert (Damaraland, rocky area in north-western Namibia)
Australia	31.33°S, 140.33°E	Australia	Australia	Strzelecki Desert

1408
1409
1410 **Table 3.** Position of LW absorption band peaks (6-16 µm) for the main minerals composing dust.
1411 Montmorillonite is taken here as representative for the smectite family. For feldspars literature data are
1412 available only for albite.

1413
1414

Mineral species	Wavelength (µm)	Reference

Illite	9.6	Querry (1987)
Kaolinite	9.0, 9.6, 9.9, 10.9	Glotch et al. (2007)
Montmorillonite	9.0, 9.6	Glotch et al. (2007)
Chlorite	10.2	Dorschner et al. (1978)
Quartz	9.2, 12.5-12.9	Peterson and Weinman (1969)
Calcite	7.0, 11.4	Long et al. (1993)
Gypsum	8.8	Long et al. (1993)
Albite	8.7, 9.1, 9.6	Laskina et al. (2012)

1415
1416
1417
1418
1419
1420
1421
1422
1423
1424
1425
1426
1427
1428
1429
1430

1431 **Figures**

1432

1433 **Figure 1.** Schematic configuration of the CESAM set up for the dust experiments. The dust generation

1434 (vibrating plate, Büchner flask containing the soil sample) and injection system is shown ~~in~~ at the bot-

1435 tom on the right side. The position of the SMPS, WELAS, and SkyGrimm used for measuring the size

1436 distribution, FTIR spectrometer, SW optical instruments, and filter sampling system are also indicated.

1437
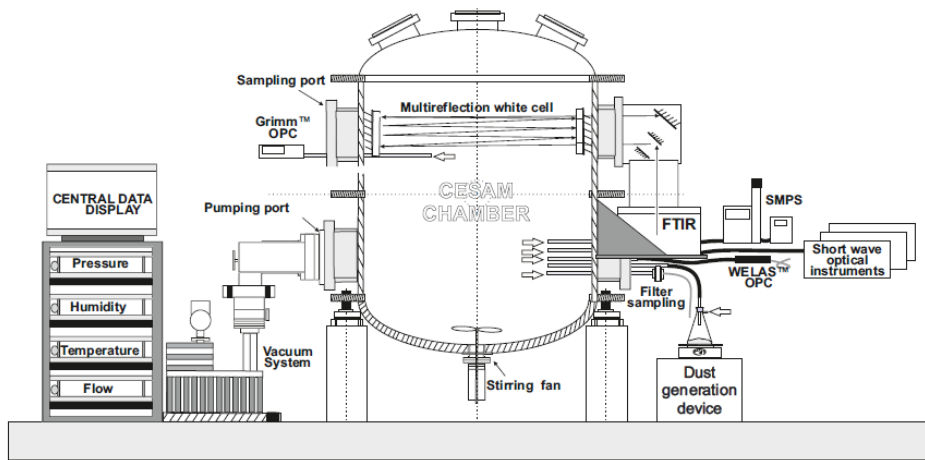
1438
1439
1440
1441

1442

1443

1444

1445

1446

1447

1448

1449

1450

1451

1452 **Figure 2.** Location (red stars) of the soil and sediment samples used to generate dust aerosols. The
1453 nine yellow rectangles depict the different global dust source areas as defined in Ginoux et al. (2012):
1454 1) Northern Africa, 2) Sahel, 3) Eastern Africa and Middle East, 4) Central Asia, 5) Eastern Asia, 6)
1455 North America, 7) South America, 8) Southern Africa, and 9) Australia.

1456
1457
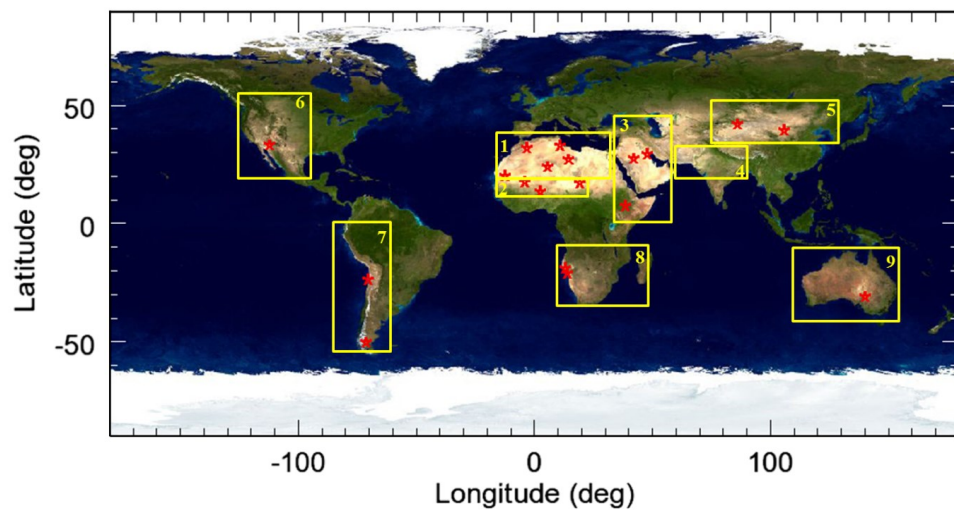
1458
1459
1460
1461
1462
1463
1464
1465
1466
1467
1468
1469
1470
1471
1472
Figure 3. Box and whisker plots showing the variability of the soil composition in the clay and silt fractions at the global scale, i.e., by considering all data from the nine dust source areas identified in Fig. 2. Data are from the soil mineralogical database by Journet et al. (2014). Dots indicate specific mineralogical characteristics (illite-to-kaolinite mass ratio, I/K, calcite and quartz contents, extracted from Journet et al.) of the soils used in the CESAM experiments, as listed in Table 2.
1478

1479

CLAY FRACTION (<2 μm)

SILT FRACTION (<60 μm)
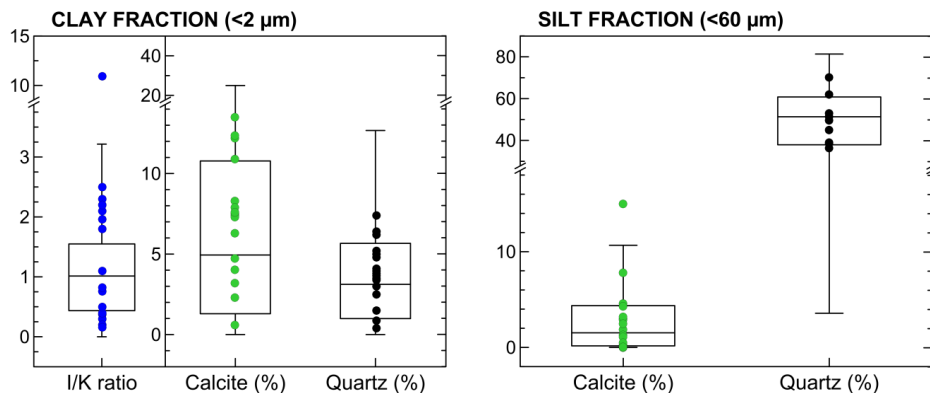
1480
1481
1482
1483
1484
1485
1486
1487
1488
1489
1490
1491
1492
1493
1494
1495
1496
1497 **Figure 4.** Mineralogy of the nineteen generated aerosol samples considered in this study, as obtained
1498 from XRD analysis. The mass apportionment between the different clay species (illite, kaolinite, chlo-
1499 rite) is shown for Northern African (Tunisia, Morocco, Libya, Mauritania, Niger, Mali, Bodélé) and
1500 Eastern Asian (Gobi, Taklimakan) aerosols based on compiled literature compiled values of the illite-
1501 to-kaolinite (I/K) and chlorite-to-kaolinite (Ch/I) mass ratios (Scheuvens et al., 2013; Formenti et al.
1502 2014). For all the other samples only the total clay mass is reported.

1503
1504
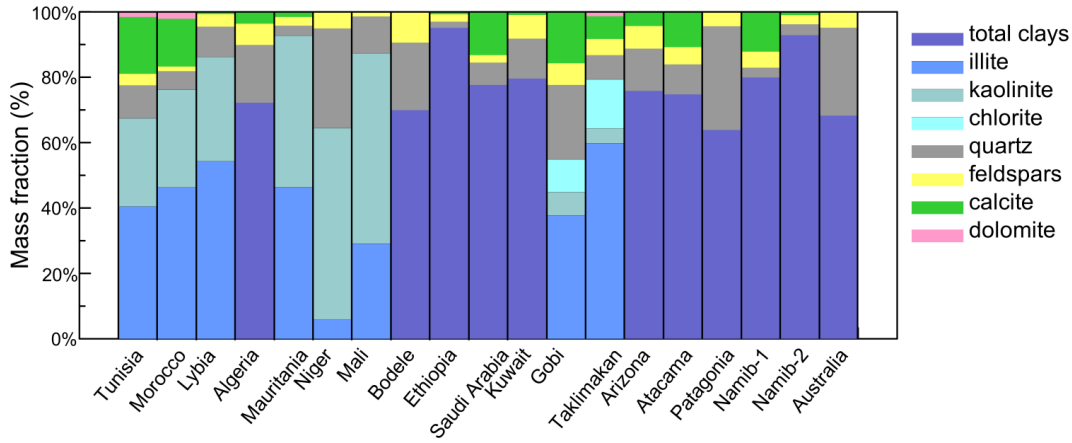
1505
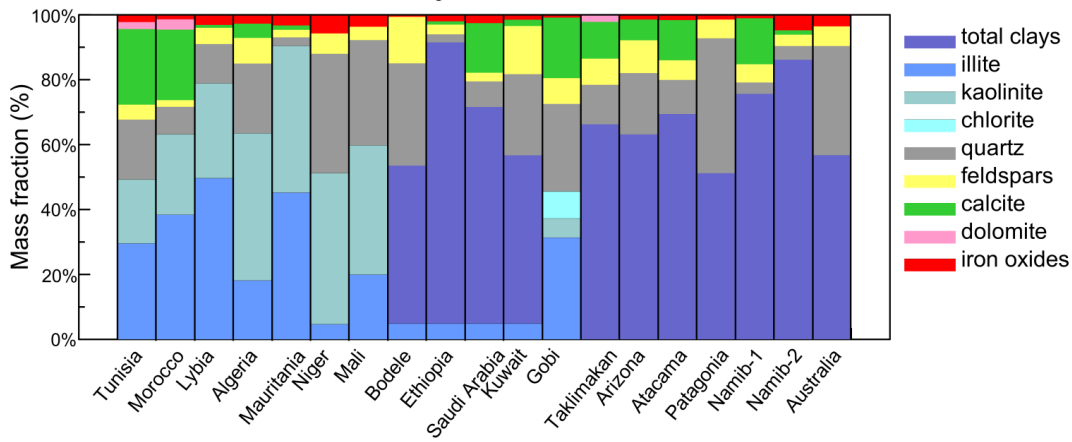
1506
1507
1508
1509
1510
1511
1512
1513
1514
1515
1516
1517
1518
1519

53

1520
1521
1522
1523
1524
1525   **Figure 5.** Surface size distributions in the CESAM chamber at the peak of dust injection for all cases

1526   ~~analysed~~analyzed in this study; the total measured dust mass concentration and the percentage of the

1527   super-micron to sub-micron number fraction at the peak are also reported in the legend.

1528
1529
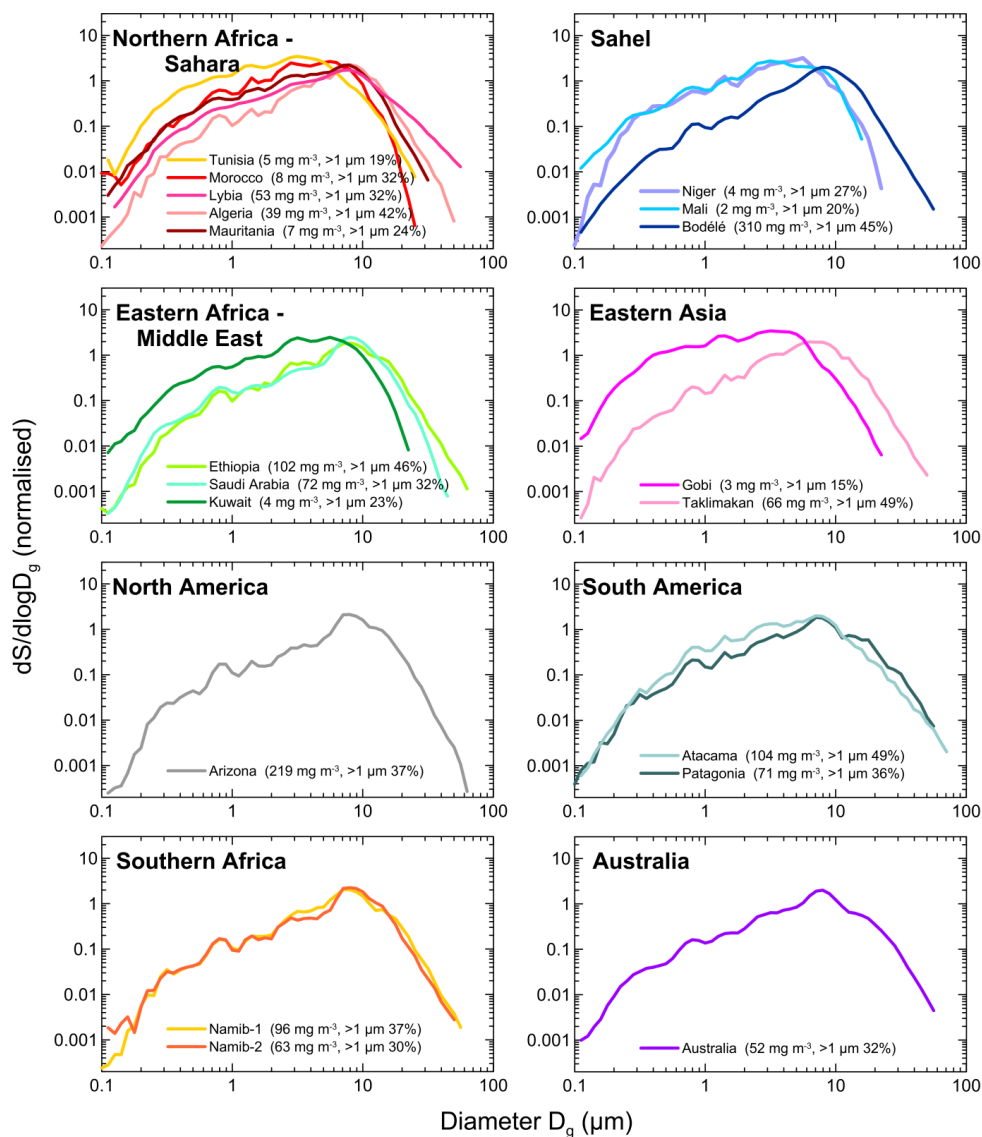
Figure 6. Comparison of CESAM measurements <u>at the peak of the injection</u> with dust size distributions from several airborne field campaigns in <u>Northern</u> Africa ~~and Asia~~. The grey shaded area represents the range of sizes measured in CESAM during experiments with the different <u>Northern African</u> <u>samples</u>~~samples~~. Data from field campaigns are: AMMA (Formenti et al., 2011), SAMUM-1 (Weinzierl et al., 2009), <u>and</u> FENNEC (Ryder et al., 2013a)~~, and ACE-Asia (Clarke et al., 2004)~~. <u>The shaded</u>

areas for each dataset~~Min and max for the same data~~ correspond to the range of variability observed for the campaigns considered.
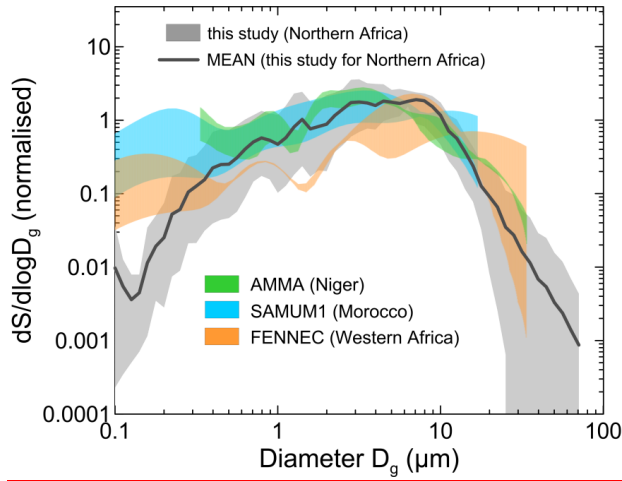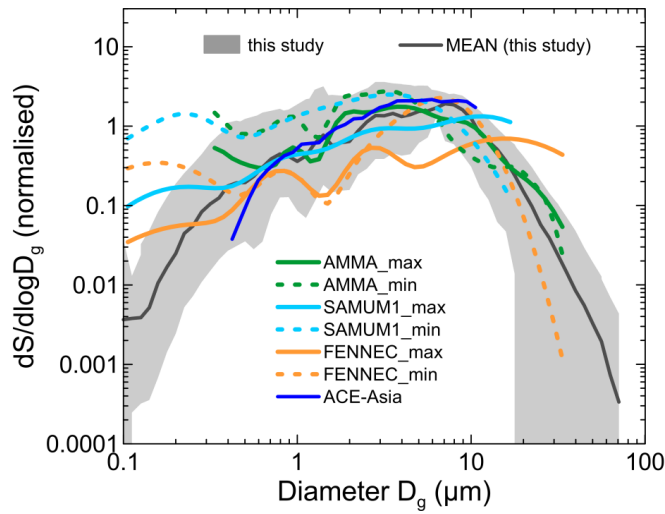
1548

1549

1550

1551

1552

1553

1554

1555

1556   **Figure 7.** Upper panel: surface size distribution measured at the peak of the dust injection and at 30,

1557   60, 90, and 120 minutes after injection for the Algeria and Atacama aerosols. The dust mass concentra-

1558   tion is also indicated in the plot. Lower panel: fraction of particles remaining airborne in the chamber

1559   as a function of time versus particle size calculated as $dN_i(D_g)/dN_0(D_g)$, where $dN_i(D_g)$ is the number

1560   of particles measured by size class at ~~the i~~ time i (i corresponding to 30, 60, 90 and 120 min after in-

1561   jection) and $dN_0(D_g)$ represents the size-dependent particle number at the peak of the injection. Values

1562   are compared to the estimate of Ryder et al. (2013b) for Saharan dust layers aged 1-2 days after emis-

1563   sion.

1564

1565
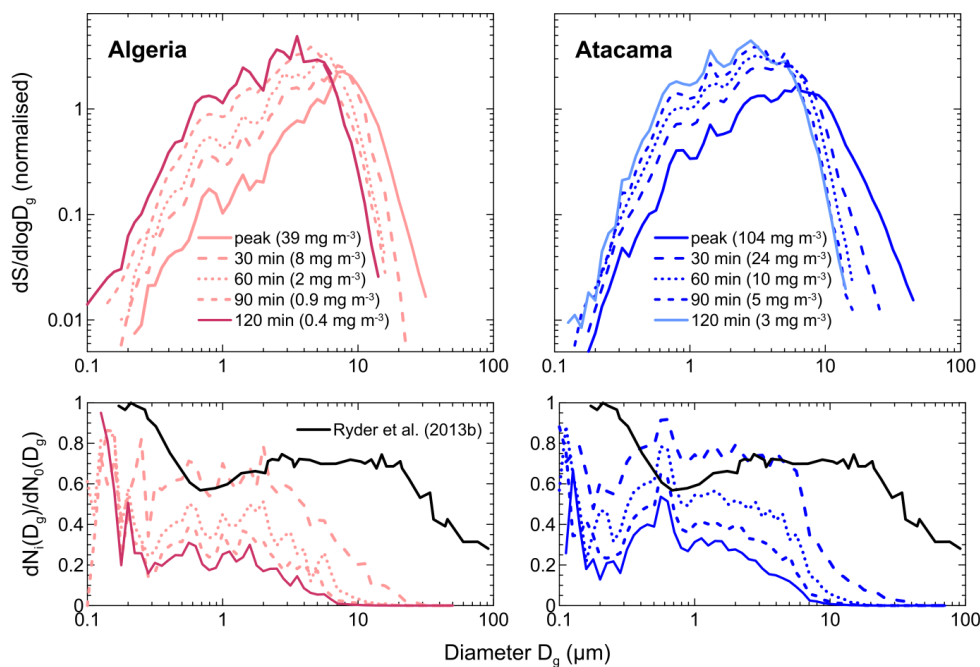
1566
1567
1568
1569
1570
1571
1572
1573
1574
1575
1576
1577

1578 **Figure 8.** Dust extinction coefficient measured in the LW spectral range for the nineteen aerosol sam-

1579 ples ~~analysed~~analyzed in this study. Data for each soil refer to the peak of the dust injection in the

1580 chamber. Note that the y-scale is different for Northern Africa – Sahara compared to the other cases.

1581 Main absorption bands by clays at 9.6 μm, quartz (Q) at 9.2 and 12.5-12.9 μm, kaolinite (K) at 10.9

1582 μm, calcite (C) at 7.0 and 11.4 μm, and feldspars (F) at 8.7 μm are also indicated in the spectra.

1583

1584

1585
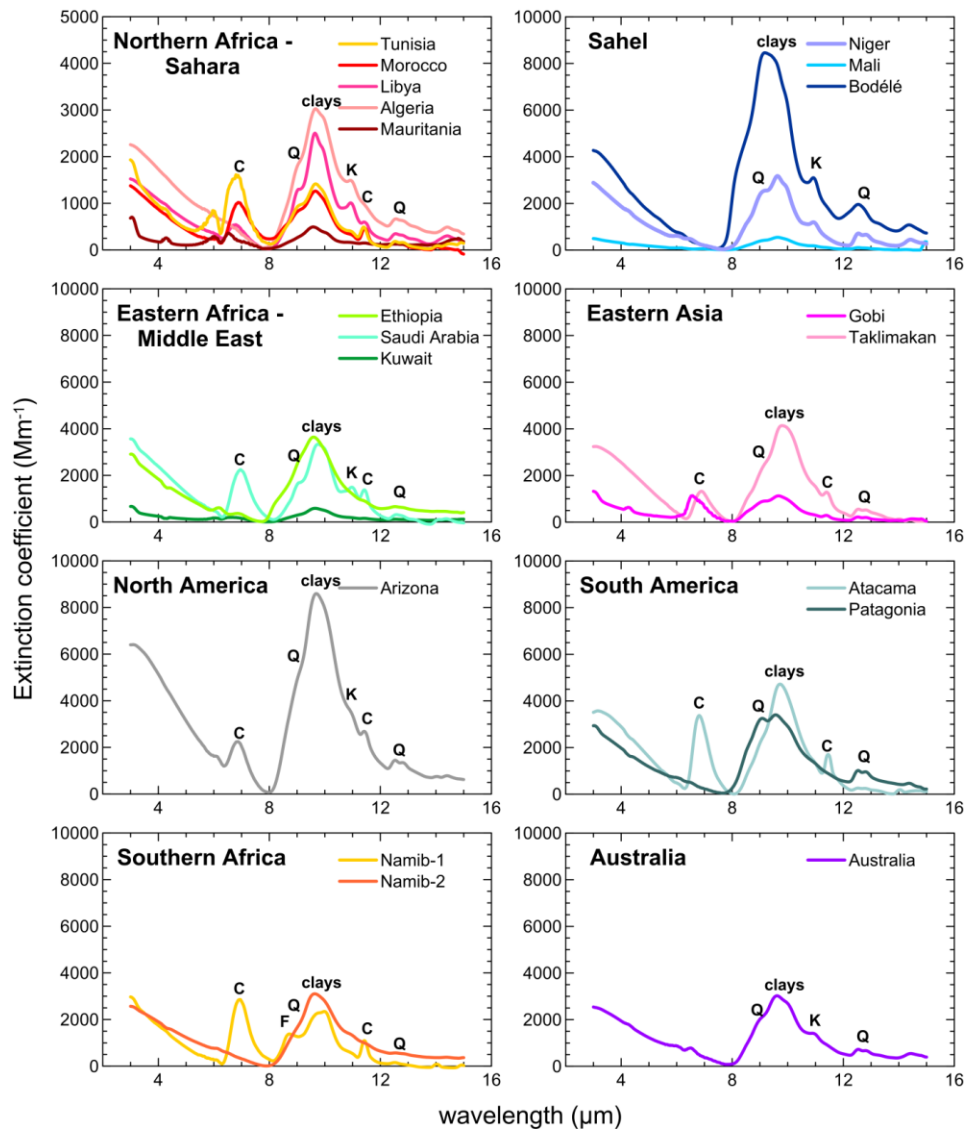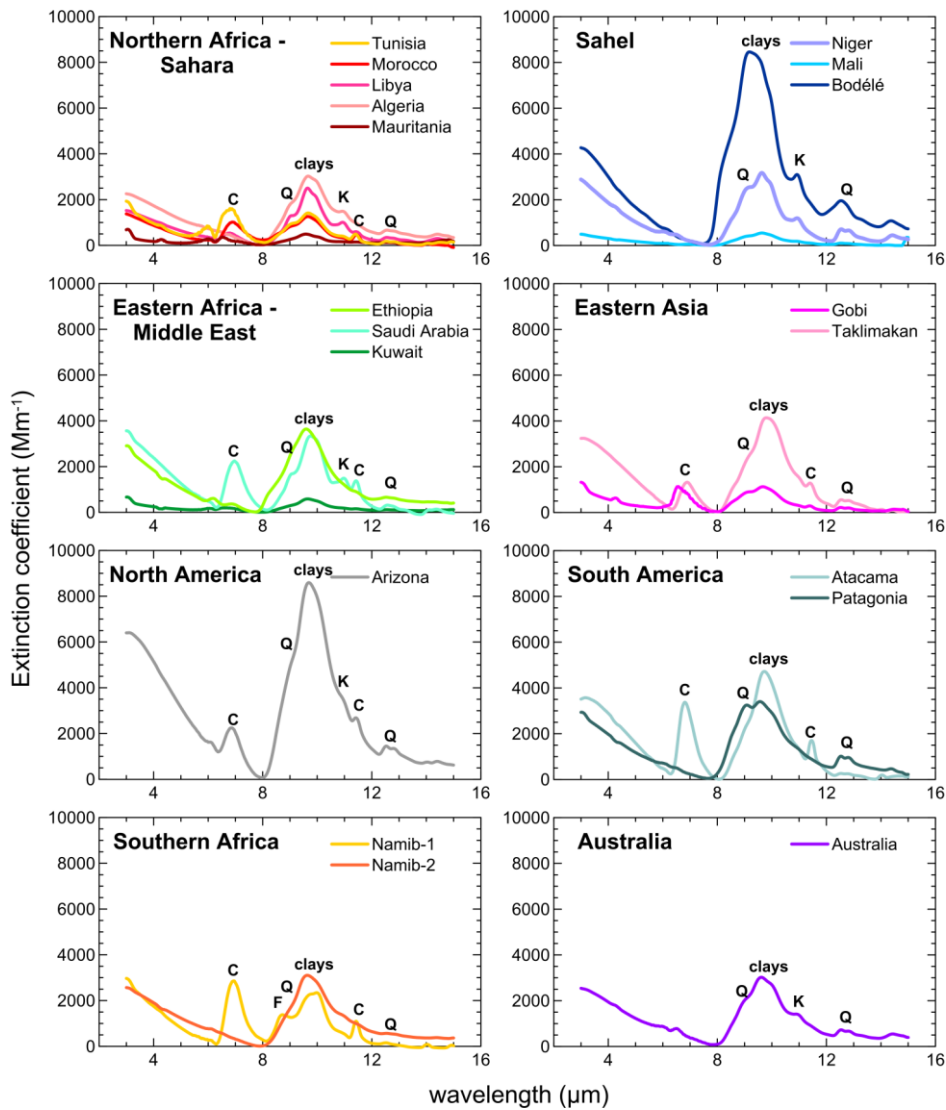
Figure 9. Extinction spectra measured at the peak of the dust injection and at 30, 60, 90, and 120 minutes after injection for the Algeria and Atacama aerosols.

60
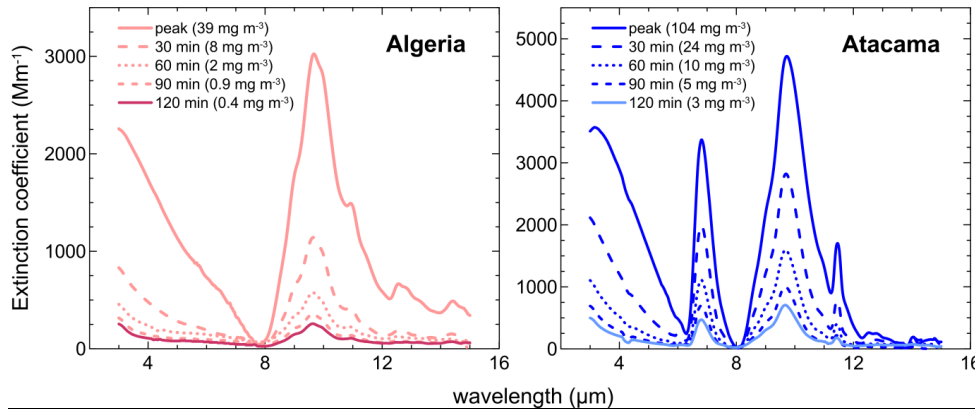
1591
1592
1593
1594
1595
1596
1597
1598
1599
1600
1601
1602
1603
1604
1605
1606
1607
1608
1609
1610
1611
1612
1613
1614
1615
1616
1617
1618
1619 **Figure 10.** Real (n) and imaginary (k) parts of the dust complex refractive index obtained for the nine-

1620 teen aerosol samples ~~analysed~~analyzed in this study. Data correspond to the time average of the 10-

1621 min values obtained between the peak of the injection and 120 min later. The error bar corresponds to

1622 the absolute uncertainty ~~on~~in n and k, estimated at ~±20%.

> **Mis en forme :** Couleur de police : Automatique, Anglais (États Unis)

61

1623

1624
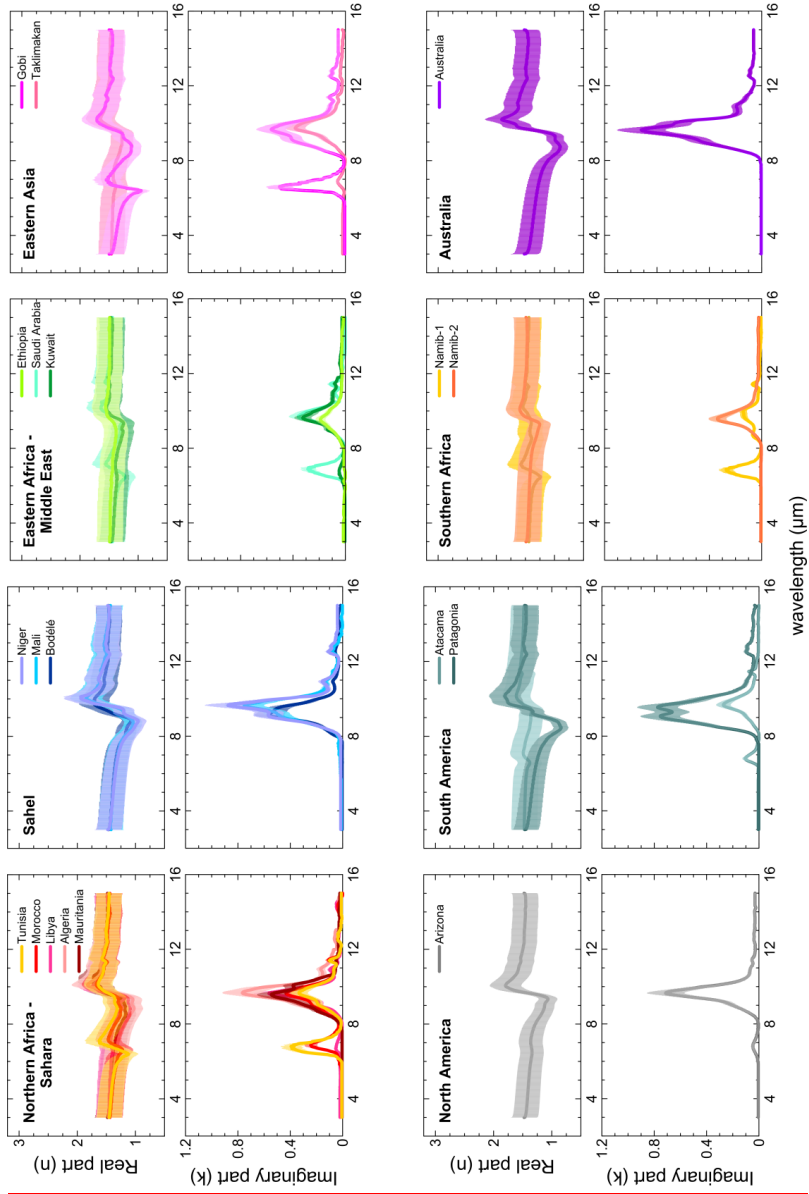
Mis en forme : Centré
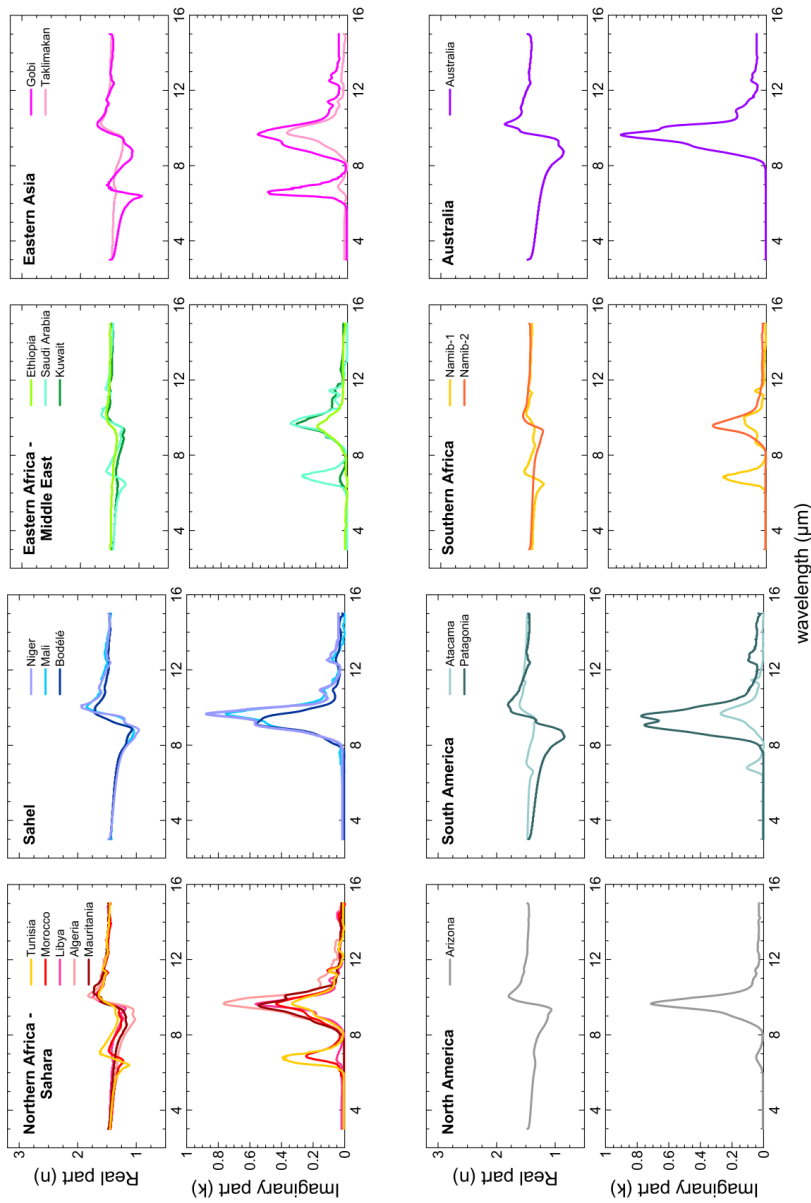
Figure 11a. Imaginary part of the complex refractive index (k) versus the mineral content (in % mass) for the bands of calcite (7.0 and 11.4 μm), quartz (9.2 μm), and clays (9.6 and 10.9 μm). For the band at 9.6 μm the plot is drawn separately for total clays, and illite and kaolinite species. The linear fits are

also reported for each plot. Linear fits were performed with the FITEXY.PRO IDL routine taking into account both x- and y-uncertainties in the data.

1634
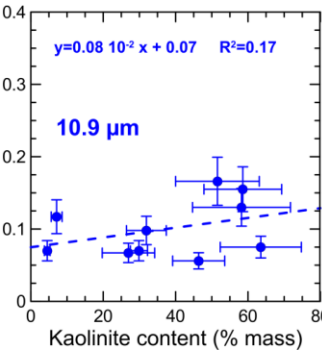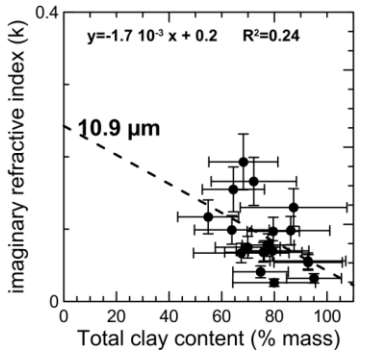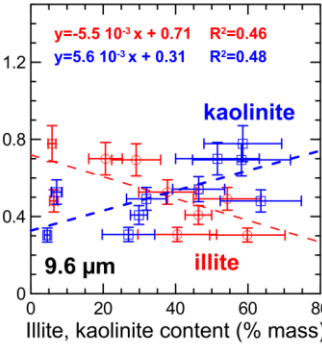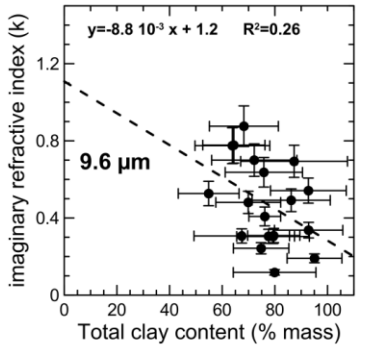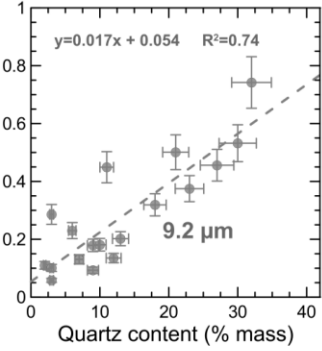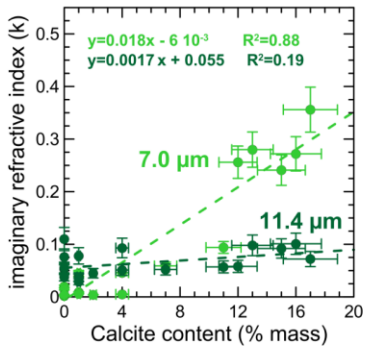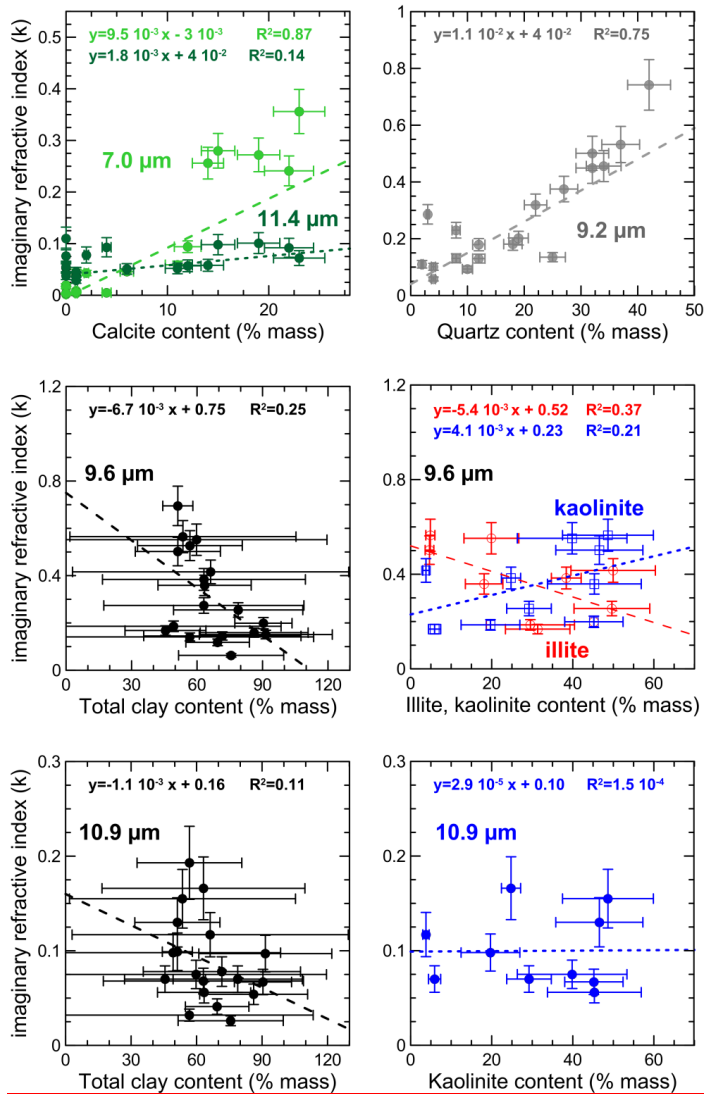
Figure 11b. Same as Fig. 11a for the real part of the complex refractive index (n).
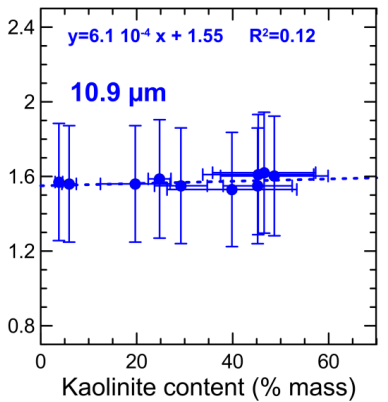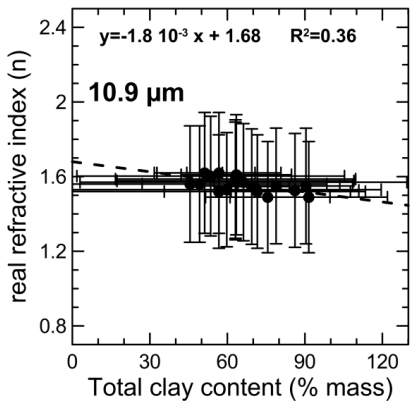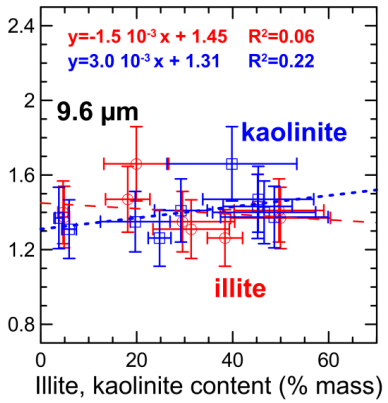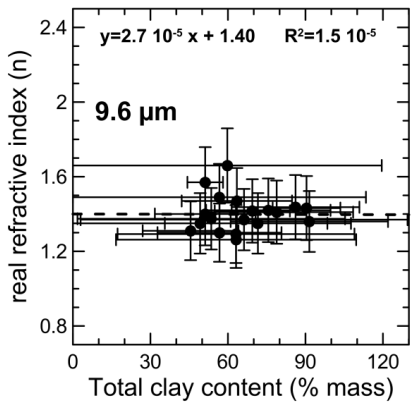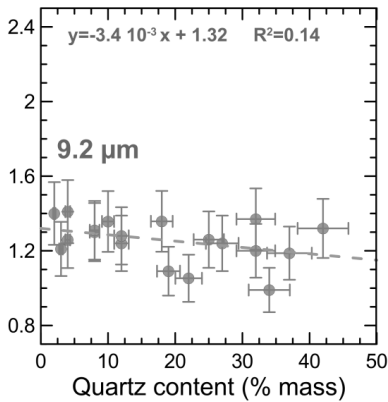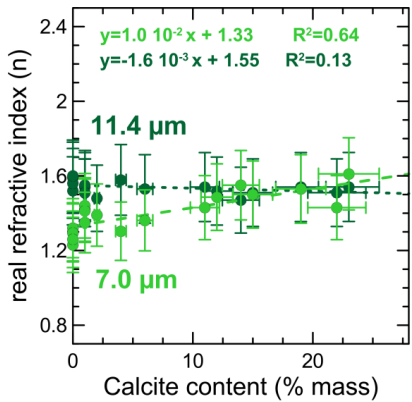
1641
1642

1643 **Figure 12.** Comparison of results obtained in this study with literature -compiled values of the dust
1644 refractive index in the LW. Literature values are taken from Volz (1972) for rainout dust collected in
1645 Germany, Volz (1973) for dust collected at Barbados, Fouquart (1987) for Niger sand, Di Biagio et al
1646 (2014a) for dust from Niger and Algeria, and the OPAC database (Hess et al., 1998). The region in
1647 gray in the plot indicates the full range of variability obtained in this study, and the dashed line is the
1648 mean of n and k obtained for the different aerosol samples. The legend in the top panel identifies the
1649 line styles used in the plot for the literature data.

1650
1651
1652
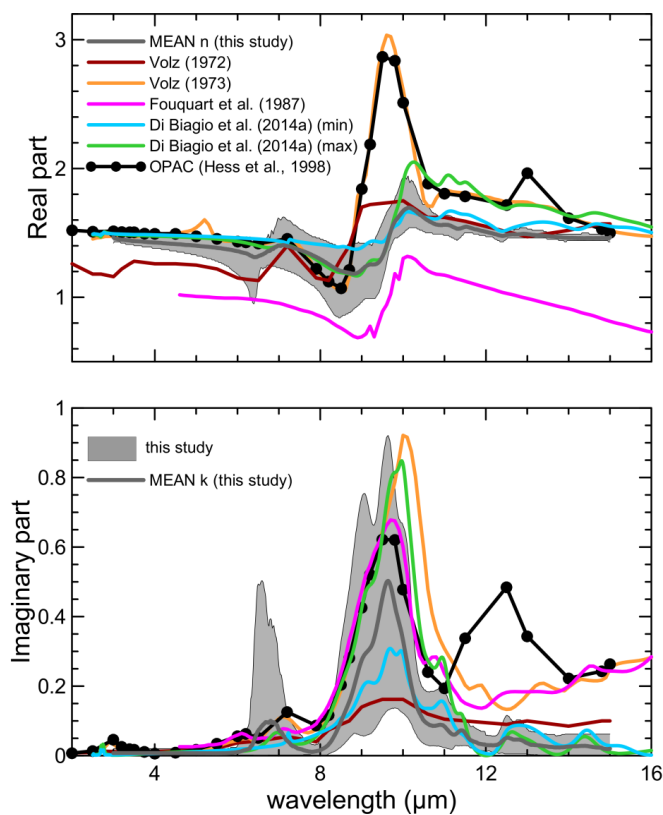
1653
1654
1655
1656
1657

Figure A1. Left panel: longwave spectrum of ammonium sulfate measured in CESAM in the 2-15 μm range. The vibrational modes $v_3(NH_4^+)$ (3230 cm^{-1} or 3.10 μm) and $v_3(SO_2^{-4})$ (1117 cm^{-1} or 8.95 μm) of ammonium sulfate are identified in the plot. Absorption bands attributed to gas-phase water vapor and CO_2 present in the chamber during experiments are also indicated. The rectangle in the plot indicates the spectral region where the retrieval of the complex refractive index was performed. Right panel: real and imaginary parts of the refractive index obtained by optical closure. The results are compared with the ammonium sulfate optical constants from Toon et al. (1976).